Monthly Notices of the ROYAL ASTRONOMICAL SOCIETY

MNRAS **515,** 5267–5284 (2022) https://doi.org/10.1093/mnras/stac2099
Advance Access publication 2022 July 28

Energy balance and Alfvén Mach numbers in compressible magnetohydrodynamic turbulence with a large-scale magnetic field

James R. Beattie [1]★ Mark R. Krumholz [1,2] Raphael Skalidis [3,4] Christoph Federrath [1,2] Amit Seta [1] Roland M. Crocker [1] Philip Mocz [5] and Neco Kriel [1]

[1] *Research School of Astronomy and Astrophysics, Australian National University, Canberra, ACT 2611, Australia*
[2] *Australian Research Council Centre of Excellence in All Sky Astrophysics (ASTRO3D), Canberra, ACT 2611, Australia*
[3] *Institute of Astrophysics, Foundation for Research and Technology – Hellas, Vasilika Vouton, GR-70013 Heraklion, Greece*
[4] *Department of Physics and ITCP, University of Crete, GR-70013 Heraklion, Greece*
[5] *Lawrence Livermore National Laboratory, 7000 East Ave, Livermore, CA 94550, USA*

Accepted 2022 July 18. Received 2022 July 16; in original form 2022 February 25

ABSTRACT

Energy equipartition is a powerful theoretical tool for understanding astrophysical plasmas. It is invoked, for example, to measure magnetic fields in the interstellar medium (ISM), as evidence for small-scale turbulent dynamo action, and, in general, to estimate the energy budget of star-forming molecular clouds. In this study, we motivate and explore the role of the volume-averaged root-mean-squared (rms) magnetic coupling term between the turbulent, $\delta\boldsymbol{B}$, and large-scale, $\boldsymbol{B}_0$, fields, $\left\langle(\delta\boldsymbol{B}\cdot\boldsymbol{B}_0)^2\right\rangle_{\mathcal{V}}^{1/2}$. By considering the second moments of the energy balance equations we show that the rms coupling term is in energy equipartition with the volume-averaged turbulent kinetic energy for turbulence with a sub-Alfvénic large-scale field. Under the assumption of exact energy equipartition between these terms, we derive relations for the magnetic and coupling term fluctuations, which provide excellent, parameter-free agreement with time-averaged data from 280 numerical simulations of compressible magnetohydrodynamic (MHD) turbulence. Furthermore, we explore the relation between the turbulent mean field and total Alfvén Mach numbers, and demonstrate that sub-Alfvénic turbulence can only be developed through a strong, large-scale magnetic field, which supports an extremely super-Alfvénic turbulent magnetic field. This means that the magnetic field fluctuations are significantly subdominant to the velocity fluctuations in the sub-Alfvénic large-scale field regime. Throughout our study, we broadly discuss the implications for observations of magnetic fields and understanding the dynamics in the magnetized ISM.

Key words: dynamo – MHD – turbulence – ISM: kinematics and dynamics – ISM: magnetic fields.

1 INTRODUCTION

Magnetohydrodynamic (MHD) turbulence is pervasive across the Universe, and for this reason the study of MHD turbulence is a necessary prerequisite for understanding a broad range of astrophysical processes. For example, each of the planets in our Solar system probably assembled as the protoplanetary disc underwent hydrodynamical and magnetohydrodynamical (MHD) instabilities, driving turbulence, and establishing the initial conditions for planet formation (Lyra & Umurhan 2019, and references therein). The Sun maintains a magnetized and turbulent heliosphere, with decades of scale-free velocity and magnetic fluctuations that play an important role in the generation of solar winds, plasma heating, and particle acceleration (Bruno & Carbone 2013, and references therein). Just like the planets, the Sun was born in a turbulent plasma environment.

In the context of star formation, turbulent density fluctuations in the cool molecular gas clouds of galaxies seed the overdensities that fragment, become gravitationally unstable, and collapse to form stars (Krumholz & McKee 2005; Hennebelle et al. 2011; Padoan & Nordlund 2011; Federrath & Klessen 2012; Hopkins 2013; Federrath 2015; Burkhart 2018; Mocz & Burkhart 2018). The turbulent motions themselves steepen or flatten the initial mass function (IMF) of stars (Padoan, Nordlund & Jones 1997; Hennebelle & Chabrier 2009; Hopkins 2012; Federrath, Krumholz & Hopkins 2017b; Nam, Federrath & Krumholz 2021) and potentially underlie the universality that we observe for the IMF by setting the density correlation scale for star-forming regions (Jaupart & Chabrier 2021), or more generally, from the universality of the supersonic turbulence energy cascade in the interstellar medium (ISM; Padoan et al. 1997; Federrath 2013). On scales above the neutral–ion decoupling scale, magnetic fields are approximately flux frozen into the gas, and fluctuate, tangle, and become turbulent with the gas velocities, hence magnetic fields also play an important role in all these processes (Hennebelle & Inutsuka 2019; Krumholz & Federrath 2019).

In the ISM magnetic fields and turbulence coexist in a partnership. Extremely weak, primordial magnetic fields were potentially formed through a battery process (e.g. Biermann 1950), or a phase transition in the early Universe (Subramanian 2016, 2019), and, once generated, they are hard to destroy due to the lack of magnetic monopoles (Parker 1970; Beck & Wielebinski 2013; Acharya et al. 2022). Instead, turbulent motions of gas exponentially amplify the weak seed fields, growing them through the turbulent dynamo, and magnetizing the plasma (see McKee, Stacy & Li 2020 for a recent

★ E-mail: james.beattie@anu.edu.au

review). Turbulence, through the dynamo process, likely continues to maintain the magnetic fields found in the present-day Universe, ensuring they are *roughly* in energy equipartition with the turbulent motions, i.e. the saturated state of the turbulent dynamo (Federrath et al. 2014; Schober et al. 2015; Federrath 2016; Xu & Lazarian 2016; McKee et al. 2020; Seta & Federrath 2020, 2021a; Seta et al. 2020; Achikanath Chirakkara et al. 2021).

Given the importance of MHD turbulence in the ISM, it is not surprising that the ISM community has built numerous tools for measuring turbulent properties (for a recent review, see Burkhart 2021). These include, but are certainly not limited to: techniques that relate starlight polarization dispersion to plane-of-sky magnetic fields strengths, such as the methods described in Skalidis & Tassis (2021), Davis (1951), and Chandrasekhar & Fermi (1953) (for recent reviews, extensions, and modifications, see Lazarian, Yuen & Pogosyan 2020, 2022); inference of magnetic field strengths and plasma energetics from local velocity centroids or intensity fluctuations (Lazarian et al. 2018) and density gradients of dust continuum maps (Soler et al. 2013); ascertaining the ratio of compressive to solenoidal modes of turbulent driving sources from the deprojected column density (Federrath, Klessen & Schmidt 2009; Brunt, Federrath & Price 2010a,b; Brunt & Federrath 2014; Körtgen & Soler 2020; Menon et al. 2021; Sharda et al. 2022); and data-driven statistical techniques that can capture abstract features of sub- or super-Alfvénic turbulence using wavelet scattering transforms (Allys et al. 2019; Saydjari et al. 2021) or deep convolutional neural networks (Peek & Burkhart 2019). All of these diagnostics rely upon a thorough physical understanding of the underlying phenomenology of MHD turbulence.

However, the parameter space of MHD turbulence is large, and there need not be a universal phenomenology that captures the richness of the topic (see the eloquent review from Schekochihin 2020 about phenomenologies and two-point statistical models for incompressible MHD turbulence, which continue to be subject to debate; Iroshnikov 1964; Kraichnan 1965; Sridhar & Goldreich 1994; Goldreich & Sridhar 1995; Boldyrev 2006). In this study, we aim to explore energy balance in a particular part of the parameter space relevant to the ISM: isothermal, highly compressible MHD turbulence, driven with a mixture of compressible and solenoidal modes, and that is threaded by a large-scale magnetic field, $\boldsymbol{B}_0$, flux frozen on the system scale. Such a description is potentially applicable to any of the approximately isothermal phases of the ISM (Wolfire et al. 1995; Omukai et al. 2005). In this context, we can identify several distinct energy reservoirs, but in this study our main aim is to understand the correlation between the large-scale and turbulent magnetic field; mathematically, this term takes the form $\delta\boldsymbol{B}\cdot\boldsymbol{B}_0$, where $\delta\boldsymbol{B}$ and $\boldsymbol{B}_0$ are the fluctuating and large-scale fields, respectively. We henceforth refer to this as the 'magnetic coupling term', or simply the 'coupling term'. This term has been neglected previously in the literature (e.g. Zweibel & McKee 1995) because when averaging over a volume $\mathcal{V}$ that contains a few turbulent correlation scales, $\langle\delta\boldsymbol{B}\cdot\boldsymbol{B}_0\rangle_{\mathcal{V}}=0$. However, we show that when one instead considers the second moments of the energy equation (the fluctuations of energy), which maintain the positivity for all of the contributions to the energy, including $\delta\boldsymbol{B}\cdot\boldsymbol{B}_0$, the coupling term plays a leading order role in the energy balance when $\boldsymbol{B}_0$ is strong, corresponding to sub-to-trans-Alfvénic turbulence.

Skalidis & Tassis (2021) and Skalidis et al. (2021a, hereafter S+2021) recently showed that the coupling term is important for measuring the plane-of-sky magnetic field using polarization dispersion techniques for interstellar gas, especially in highly magnetized regions of the ISM (Li et al. 2013; Federrath et al. 2016; Hu et al. 2019; Heyer, Soler & Burkhart 2020; Hwang et al. 2021; Skalidis et al. 2021b; Hoang et al. 2022). In this paper, we show that by constructing a set of analytical models for the coupling term and turbulent magnetic fluctuations, based on kinetic and magnetic energy balance, one can derive strong constraints on the magnetic fluctuations and Alfvén Mach numbers $\mathcal{M}_{\rm A}$ in the plasma. We also study the impact of a large-scale magnetic field on the turbulence by analysing the turbulent, total and mean field $\mathcal{M}_{\rm A}$, and the relationships between them. Beyond significantly suppressing the turbulent component of the magnetic field as the large-scale field grows in energy in a power-law fashion, $\delta B\propto B_0^{-1}$, we show that having a strong large-scale field is a necessary prerequisite for sub-Alfvénic turbulence, i.e. a plasma can only be in the sub-Alfvénic regime when the large-scale ordered field contains almost all of the magnetic energy, making the magnetic fluctuations highly super-Alfvénic and hence dynamically subdominant.

This study is organized as follows. In Section 2, we outline the compressible MHD turbulence simulations that we will use. In Section 3, we review the basics of energy balance between magnetic and kinetic energy in MHD turbulence. We focus upon the coupling term, justify why it ought to be considered in the energy balance equation,. and in Section 4, we provide analytical models for this term in both the super- and sub-Alfvénic regimes. In Section 5, we turn our attention to the fluid energetics in the context of the Alfvén Mach number, highlighting the difference between the turbulent mean field and total Alfvén Mach numbers and deriving relationships between them. Next, in Section 6, we discuss the role of the turbulent correlation scale for measuring magnetic field statistics in simulations and observations. Finally, in Section 7, we summarize the key results of this study.

2 NUMERICAL SIMULATIONS

To test our energy balance models, we use a modified version of the FLASH code (Fryxell et al. 2000; Dubey et al. 2008), utilizing a second-order conservative MUSCL-Hancock 5-wave approximate Riemann scheme (Bouchut, Klingenberg & Waagan 2010; Waagan, Federrath & Klingenberg 2011; Federrath et al. 2021) to solve the 3D, ideal, isothermal, compressible MHD equations with a stochastic acceleration field acting to drive non-helical turbulence,

$$\frac{\partial\rho}{\partial t}+\nabla\cdot(\rho\boldsymbol{v})=0, \tag{1}$$

$$\rho\frac{\partial\boldsymbol{v}}{\partial t}-\nabla\cdot\left[\frac{1}{4\pi}\boldsymbol{B}\otimes\boldsymbol{B}-\rho\boldsymbol{v}\otimes\boldsymbol{v}-\left(c_{\rm s}^2\rho+\frac{B^2}{8\pi}\right)\mathbb{I}\right]=\rho\boldsymbol{f}, \tag{2}$$

$$\frac{\partial\boldsymbol{B}}{\partial t}-\nabla\times(\boldsymbol{v}\times\boldsymbol{B})=0, \tag{3}$$

$$\nabla\cdot\boldsymbol{B}=0, \tag{4}$$

where $\otimes$ is the tensor product and $\mathbb{I}$ the identity matrix. We solve the equations on a periodic domain of dimension $L^3\equiv\mathcal{V}_L$, discretized with between 16^3 and 1152^3 cells, where $\boldsymbol{v}$ is the fluid velocity, ρ is the gas density, $\boldsymbol{B}=B_0\hat{\boldsymbol{e}}_\parallel+\delta\boldsymbol{B}(t)$ is the magnetic field, with mean-field $B_0\hat{\boldsymbol{e}}_\parallel$[1] and turbulent field $\delta\boldsymbol{B}(t)$, where $\langle\delta\boldsymbol{B}(t)\rangle_{\mathcal{V}_L}=0$, $c_{\rm s}$ is the sound speed, and $\boldsymbol{f}$ the stochastic turbulent acceleration source term that drives the turbulence, which, in the ISM could be

[1]Note that we refer to a mean-field coordinate system, as adopted in Hartlep et al. (2000), where $\boldsymbol{B}_0$ always points along $\hat{\boldsymbol{z}}=\hat{\boldsymbol{e}}_\parallel$ and hence $\hat{\boldsymbol{x}}=\hat{\boldsymbol{e}}_{\perp,1}$ and $\hat{\boldsymbol{y}}=\hat{\boldsymbol{e}}_{\perp,2}$. The plasma is statistically symmetric in the $(\hat{\boldsymbol{e}}_{\perp,1},\hat{\boldsymbol{e}}_{\perp,2})$ plane, so we will regularly state quantities for $\hat{\boldsymbol{e}}_\perp$.

from, for example, supernova shocks, internal instabilities in the gas, gravity, galactic-scale shocks and shear, or ambient pressure from the galactic environment (Brunt, Heyer & Mac Low 2009; Elmegreen 2009; Federrath 2015; Krumholz & Burkhart 2016; Padoan et al. 2016; Federrath et al. 2017a; Grisdale et al. 2017; Jin et al. 2017; Körtgen, Federrath & Banerjee 2017; Colling et al. 2018; Schruba, Kruijssen & Leroy 2019; Lu et al. 2020). Here, and throughout this paper, we use the notation $\langle\cdots\rangle_{\mathcal{V}}$ to indicate the mean value of some quantity within a specified volume $\mathcal{V}$ (which can be the entire simulation volume $\mathcal{V}_L$, but need not be). We discuss the resolution of our simulations, and demonstrate that the quantities of interest for us are converged in them, in Appendix A.

The forcing term $\boldsymbol{f}$ follows an Ornstein–Uhlenbeck process with finite correlation time, $\tau = \ell_0/\langle v^2\rangle_{\mathcal{V}_L}^{1/2} = L/(2c_s\mathcal{M})$, where $\mathcal{M}$ is the sonic Mach number, such that $\ell_0 = L/2$ is the driving, or energy injection scale, and $\boldsymbol{f}$ is constructed so that we are able to set $0.5 \lesssim \mathcal{M} \lesssim 10$, encapsulating the $\mathcal{M}$ values of supersonic molecular gas clouds in the ISM (e.g. Schneider et al. 2013; Federrath et al. 2016; Orkisz et al. 2017; Beattie et al. 2019) and the subsonic, diffuse, warm medium (e.g. Kritsuk, Ustyugov & Norman 2017). We force with equal energy in both compressive ($\nabla\times\boldsymbol{f}=0$) and solenoidal ($\nabla\cdot\boldsymbol{f}=0$) modes. The energy injection is isotropic, centred on $|\boldsymbol{k}L/2\pi| = 2$ and falling off to zero with a parabolic spectrum within $1 \le |\boldsymbol{k}L/2\pi| \le 3$ (see Federrath, Klessen & Schmidt 2008; Federrath et al. 2009, 2010, 2022 for turbulence driving details). $\mathcal{M}_{\rm A0}$ is set by fixing B_0 and using the definition of the mean-field Alfvén velocity and $\mathcal{M}$, $\mathcal{M}_{\rm A0} = 2c_s\sqrt{\pi\rho_0}\mathcal{M}/B_0$. We vary this value for each of the simulations in the range $10^{-2} \lesssim \mathcal{M}_{\rm A0} \lesssim 10^3$, resulting in a total of 280 simulations across different grid resolutions, with 56 unique simulations, which we list in Table 1. The initial velocity field is set to $\boldsymbol{v}(x,y,z,t=0)=\boldsymbol{0}$, with units $c_s=1$, the density field $\rho(x,y,z,t=0)=\rho_0$, with units $\rho_0=1$, and $\delta\boldsymbol{B}(t=0)=\boldsymbol{0}$, with units $c_s\rho_0^{1/2}=1$.

We run the simulations for 10 correlation times of $\boldsymbol{f}$, and report statistics from time-averages over the last five correlation times to ensure that the sub-Alfvénic mean-field simulations are statistically stationary (Beattie et al. 2021b). After five correlation times large vertical structures develop in the sub-Alfvénic mean-field simulations, extending along the strong large-scale field and out to the driving scale perpendicular to the field, which we show, as an example, in Fig. 1 for the `M2MA01` simulation.[2] For more details about the current simulations, we refer the readers to Beattie & Federrath (2020) for the anisotropy in ρ/ρ_0, Beattie, Federrath & Seta (2020) for a detailed analysis of $\delta\boldsymbol{B}$, Beattie et al. (2021a) for an anisotropic model of the ρ/ρ_0 variance, and Beattie et al. (2021b) for the density intermittency and the $\ln(\rho/\rho_0)$ probability density function (PDF).

3 ENERGY BALANCE

3.1 Energy balance basics and averaging

Recent studies have shown that one can use energy balance arguments that include the large-scale magnetic field, $\boldsymbol{B}_0$, to derive scaling laws between the Alfvénic and kinetic fluid quantities (Federrath 2016; Beattie et al. 2020; Skalidis & Tassis 2021; S+2021). The dimensionless magnetic energy density, by which we mean the magnetic energy density normalized to the mean thermal pressure[3] $\rho_0 c_s^2$, is

$$e_{\rm mag} = \frac{B^2}{8\pi c_s^2\rho_0} = \frac{1}{8\pi c_s^2\rho_0}\left(B_0^2 + \underbrace{2\delta\boldsymbol{B}\cdot\boldsymbol{B}_0}_{\text{coupling term}} + \delta B^2\right), \tag{5}$$

where B_0^2 is the large-scale field contribution to the total energy, δB^2 is the turbulent field contribution, and $2\delta\boldsymbol{B}\cdot\boldsymbol{B}_0$ is the coupling term between the two field components. In the linear perturbation theory limit of the MHD equations, δB^2 includes contributions from shear Alfvén, fast and slow magnetosonic compressive eigenmodes (e.g. Landau & Lifshitz 1959). Because $\delta\boldsymbol{B}\cdot\boldsymbol{B}_0 = \delta B_\parallel B_0$, the coupling term only contains the component of magnetic field fluctuations that are parallel to the large-scale field. In linear theory, both fast and slow magnetosonic compressible modes are able to perturb the field variables parallel to $\boldsymbol{B}_0$, so under the lens of linear theory, the coupling term is the fluctuation contribution from the compressible modes in the turbulence scaled by B_0 (Bhattacharjee, Ng & Spangler 1998). Furthermore, for sub-Alfvénic turbulence Beattie et al. (2021b) showed that converging, shocked flows along magnetic field lines excite strong $\delta B_\parallel$ fluctuations, which travel roughly at the theoretical fast Alfvén mode speed. Therefore, it is likely, assuming that $\delta B_\parallel/B_0 \ll 1$ (this is indeed the case for $\mathcal{M}_{\rm A0} < 1$ plasmas; see left panel of fig. 5 in Beattie et al. 2022) where a linear theory may be valid for the magnetic field, the coupling term contains significant energy contributions from fast magnetosonic modes excited by shocked gas that converges and forms dense filaments perpendicular to magnetic field lines.

The excitation of a dominating $\delta B_\parallel$ is something characteristic of sub-Alfvénic compressible turbulence. We demonstrate this by plotting the time-averaged joint $\delta B_\parallel$–$\delta B_\perp$ PDF in Fig. 2, for highly sub-Alfvénic turbulence ($\mathcal{M}_{\rm A0}=0.01$). It is evident that the distributions of $\delta B_\parallel$ and $\delta B_\perp$ are not the same.[4] The reason is straightforward: $\delta B_\perp$ (fluctuations from shear Alfvén waves) is subject to a quadratic restoring force via the magnetic tension[5] (Yuen & Lazarian 2020; Beattie et al. 2021b), which results in a symmetry about $\delta B_\perp = 0$. However, $\delta B_\parallel$ has a linear restoring force and is forced out of the minimum energy state $\delta B_\parallel = -B_0$ to conform to $\langle\delta B_\parallel\rangle_{\mathcal{V}} = 0$[6] (S+2021). This gives rise to a skewed distribution in $\delta B_\parallel$, with a long extended tail of negative $\delta B_\parallel$ values. We will show below that $\delta B_\parallel$ contains almost all of the turbulent magnetic energy in the compressible plasma. Now we turn our attention to what feeds the magnetic field fluctuations.

[2] We use a naming convention for our simulations whereby the value following the `M` gives the target sonic Mach number $\mathcal{M}$ (with decimal points omitted) and the value following `MA` gives the target Alfvén Mach number $\mathcal{M}_{\rm A0}$ – thus run `M2MA01` is one where we set the mean magnetic field and tune the forcing to produce $\mathcal{M}=2$ and $\mathcal{M}_{\rm A0}=0.1$.

[3] A natural normalization for an isothermal plasma because ρ_0 and c_s are both constant, and problem dependent.

[4] We show the super-Alfvénic version of this plot, which admits to isotropic fluctuations, in Fig. B3.

[5] When $B_0 \gg \delta B$, $(\boldsymbol{B}\cdot\nabla)\boldsymbol{B} \approx -\kappa B_0^2\hat{\boldsymbol{e}}_\perp$, where κ is the field line curvature. Hence $(\boldsymbol{B}\cdot\nabla)\boldsymbol{B}$ acts to strongly dampen shear Alfvén waves. This approximation for $(\boldsymbol{B}\cdot\nabla)\boldsymbol{B}$ is most appropriate for regions of the plasma where $\nabla_\parallel \cdot v_\parallel \approx 0$, because compressions can excite $\delta B_\parallel$, creating parallel gradients in the magnetic field that also act to increase the tension (Beattie et al. 2021b).

[6] Note that in the language of solid-state physics, we may consider $\delta B_\parallel$ to be a topologically frustrated field, because the minimum energy state is $\delta B_\parallel = -B_0$, but conservation of total magnetic flux requires $\langle\delta B_\parallel\rangle_{\mathcal{V}} = 0$. Hence, populations of parallel magnetic fluctuations can be imagined to compete to get to $\delta B_\parallel = -B_0$, but for every $\delta B_\parallel$ that comes close to $-B_0$ there must be either another fluctuation that comes close to $+B_0$ or a population of fluctuations that in total add to $+B_0$, ensuring globally that $\langle\delta B_\parallel\rangle_{\mathcal{V}} = 0$. We do not take this analogy any further in this study but it may stimulate future works on magnetic field fluctuation PDFs.

Table 1. Main simulation parameters and derived quantities used throughout this study.

	Turbulence		Large-scale $\boldsymbol{B}$-field		Fluctuating $\boldsymbol{B}$-field			Total $\boldsymbol{B}$-field
Simulation ID	$\mathcal{M}$	$\frac{\ell_{\mathrm{cor},v}}{\ell_0}$	$\mathcal{M}_{\mathrm{A0}}$	$\frac{B_0}{c_{\mathrm{s}}\rho_0^{1/2}}$	$\left\langle \frac{\delta B^2}{c_{\mathrm{s}}^2\rho_0} \right\rangle_{\mathcal{V}}$	$\left\langle \left(\frac{\delta \boldsymbol{B}\cdot\boldsymbol{B}_0}{c_{\mathrm{s}}^2\rho_0} \right)^2 \right\rangle_{\mathcal{V}}^{1/2}$	$\mathcal{M}_{\mathrm{A,turb}}$	$\mathcal{M}_{\mathrm{A,total}}$
(1)	(2)	(3)	(4)	(5)	(6)	(7)	(8)	(9)
M05MA001	$0.567^{+0.02}_{-0.07}$	$1.48^{+0.05}_{-0.07}$	$0.0113^{+0.0003}_{-0.001}$	177.0	$0.000191^{+0.004}_{-0.005}$	$2.32^{+0.4}_{-0.5}$	$392.0^{+20.0}_{-40.0}$	$0.0113^{+0.0003}_{-0.001}$
M05MA01	$0.566^{+0.02}_{-0.07}$	$1.47^{+0.05}_{-0.07}$	$0.113^{+0.004}_{-0.01}$	17.7	$0.0181^{+0.03}_{-0.04}$	$2.23^{+0.3}_{-0.4}$	$35.6^{+2.0}_{-2.0}$	$0.113^{+0.004}_{-0.01}$
M05MA05	$0.534^{+0.004}_{-0.04}$	$1.44^{+0.02}_{-0.07}$	$0.534^{+0.004}_{-0.04}$	3.54	$0.233^{+0.05}_{-0.08}$	$1.16^{+0.05}_{-0.1}$	$7.28^{+0.3}_{-0.2}$	$0.544^{+0.005}_{-0.05}$
M05MA1	$0.469^{+0.01}_{-0.05}$	$0.953^{+0.02}_{-0.005}$	$0.938^{+0.03}_{-0.1}$	1.77	$1.2^{+0.1}_{-0.3}$	$1.0^{+0.08}_{-0.07}$	$2.75^{+0.1}_{-0.2}$	$0.974^{+0.07}_{-0.08}$
M05MA2	$0.462^{+0.03}_{-0.03}$	$0.783^{+0.06}_{-0.03}$	$1.85^{+0.1}_{-0.1}$	0.886	$3.17^{+0.3}_{-0.3}$	$0.871^{+0.03}_{-0.07}$	$1.67^{+0.2}_{-0.08}$	$1.59^{+0.2}_{-0.09}$
M05MA4	$0.473^{+0.06}_{-0.03}$	$0.838^{+0.03}_{-0.03}$	$3.79^{+0.5}_{-0.2}$	0.443	$3.12^{+0.2}_{-0.2}$	$0.415^{+0.02}_{-0.009}$	$1.98^{+0.2}_{-0.2}$	$2.1^{+0.4}_{-0.2}$
M05MA6	$0.483^{+0.06}_{-0.03}$	$0.904^{+0.03}_{-0.03}$	$5.8^{+0.8}_{-0.4}$	0.295	$2.74^{+0.09}_{-0.1}$	$0.256^{+0.01}_{-0.006}$	$2.32^{+0.4}_{-0.1}$	$2.51^{+0.5}_{-0.2}$
M05MA8	$0.502^{+0.06}_{-0.02}$	$0.907^{+0.05}_{-0.02}$	$8.03^{+1.0}_{-0.3}$	0.222	$2.47^{+0.1}_{-0.2}$	$0.192^{+0.009}_{-0.01}$	$2.76^{+0.3}_{-0.1}$	$2.99^{+0.3}_{-0.2}$
M05MA10	$0.514^{+0.06}_{-0.03}$	$0.934^{+0.02}_{-0.03}$	$10.3^{+1.0}_{-0.5}$	0.177	$2.24^{+0.1}_{-0.07}$	$0.145^{+0.01}_{-0.006}$	$3.05^{+0.4}_{-0.2}$	$3.18^{+0.4}_{-0.1}$
M05MA100	$0.637^{+0.09}_{-0.05}$	$0.889^{+0.04}_{-0.03}$	$127.0^{+20.0}_{-10.0}$	0.0177	$0.721^{+0.1}_{-0.3}$	$0.00852^{+0.0008}_{-0.001}$	$7.9^{+3.0}_{-1.0}$	$7.92^{+3.0}_{-1.0}$
M05MA1000	$0.672^{+0.07}_{-0.05}$	$0.835^{+0.03}_{-0.04}$	$1340.0^{+100.0}_{-100.0}$	0.00177	$0.36^{+0.2}_{-0.3}$	$0.000613^{+0.0001}_{-0.0002}$	$11.8^{+8.0}_{-3.0}$	$11.8^{+8.0}_{-3.0}$
M2MA001	$1.9^{+0.04}_{-0.06}$	$1.34^{+0.02}_{-0.09}$	$0.0095^{+0.0002}_{-0.0003}$	709.0	$0.000879^{+0.02}_{-0.003}$	$18.7^{+9.0}_{-2.0}$	$498.0^{+20.0}_{-30.0}$	$0.00943^{+0.0002}_{-0.0003}$
M2MA01	$1.85^{+0.06}_{-0.02}$	$1.37^{+0.03}_{-0.1}$	$0.0926^{+0.003}_{-0.001}$	70.9	$0.0989^{+0.1}_{-0.03}$	$18.4^{+4.0}_{-1.0}$	$41.1^{+2.0}_{-3.0}$	$0.0917^{+0.003}_{-0.001}$
M2MA05	$2.24^{+0.07}_{-0.09}$	$1.26^{+0.08}_{-0.06}$	$0.561^{+0.02}_{-0.02}$	14.2	$6.81^{+0.3}_{-0.3}$	$20.6^{+3.0}_{-2.0}$	$5.28^{+0.3}_{-0.3}$	$0.575^{+0.01}_{-0.03}$
M2MA1	$1.98^{+0.1}_{-0.09}$	$0.845^{+0.02}_{-0.02}$	$0.989^{+0.05}_{-0.05}$	7.09	$25.3^{+0.3}_{-1.0}$	$16.3^{+0.7}_{-1.0}$	$2.47^{+0.2}_{-0.2}$	$1.01^{+0.05}_{-0.06}$
M2MA2	$1.95^{+0.2}_{-0.2}$	$0.815^{+0.04}_{-0.04}$	$1.95^{+0.2}_{-0.2}$	3.54	$40.6^{+0.6}_{-0.9}$	$12.3^{+0.7}_{-1.0}$	$1.73^{+0.4}_{-0.07}$	$1.54^{+0.1}_{-0.1}$
M2MA4	$2.07^{+0.2}_{-0.1}$	$0.92^{+0.02}_{-0.04}$	$4.13^{+0.5}_{-0.3}$	1.77	$37.0^{+0.3}_{-0.3}$	$5.88^{+0.4}_{-0.3}$	$2.39^{+0.1}_{-0.4}$	$2.39^{+0.3}_{-0.4}$
M2MA6	$2.09^{+0.2}_{-0.2}$	$0.946^{+0.02}_{-0.05}$	$6.26^{+0.6}_{-0.6}$	1.18	$33.8^{+0.5}_{-0.4}$	$3.83^{+0.1}_{-0.1}$	$2.45^{+0.5}_{-0.3}$	$2.68^{+0.6}_{-0.5}$
M2MA8	$2.05^{+0.09}_{-0.2}$	$0.945^{+0.04}_{-0.02}$	$8.21^{+0.4}_{-0.7}$	0.886	$21.5^{+0.3}_{-0.3}$	$2.39^{+0.1}_{-0.1}$	$3.44^{+0.2}_{-0.3}$	$3.91^{+0.2}_{-0.3}$
M2MA10	$2.11^{+0.1}_{-0.2}$	$0.987^{+0.03}_{-0.03}$	$10.5^{+0.7}_{-1.0}$	0.709	$18.4^{+0.3}_{-0.1}$	$1.74^{+0.1}_{-0.04}$	$4.07^{+0.3}_{-0.6}$	$4.65^{+0.4}_{-0.9}$
M2MA100	$2.36^{+0.1}_{-0.2}$	$1.01^{+0.03}_{-0.02}$	$118.0^{+6.0}_{-8.0}$	0.0709	$3.3^{+0.08}_{-0.5}$	$0.0729^{+0.003}_{-0.006}$	$16.1^{+3.0}_{-2.0}$	$17.0^{+4.0}_{-3.0}$
M2MA1000	$2.37^{+0.08}_{-0.1}$	$0.999^{+0.01}_{-0.05}$	$1180.0^{+40.0}_{-70.0}$	0.00709	$0.276^{+0.3}_{-0.3}$	$0.00214^{+0.0005}_{-0.0007}$	$61.9^{+40.0}_{-20.0}$	$62.8^{+40.0}_{-20.0}$
M4MA01	$4.03^{+0.06}_{-0.5}$	$1.39^{+0.05}_{-0.09}$	$0.101^{+0.002}_{-0.01}$	142.0	$0.838^{+0.2}_{-0.4}$	$106.0^{+9.0}_{-20.0}$	$36.5^{+3.0}_{-3.0}$	$0.1^{+0.002}_{-0.01}$
M4MA05	$4.08^{+0.04}_{-0.1}$	$1.27^{+0.04}_{-0.1}$	$0.51^{+0.005}_{-0.01}$	28.4	$24.4^{+0.4}_{-0.6}$	$74.1^{+7.0}_{-7.0}$	$4.94^{+0.3}_{-0.4}$	$0.513^{+0.007}_{-0.01}$
M4MA1	$4.12^{+0.5}_{-0.4}$	$0.832^{+0.04}_{-0.04}$	$1.03^{+0.1}_{-0.09}$	14.2	$84.3^{+2.0}_{-2.0}$	$61.9^{+7.0}_{-10.0}$	$2.49^{+0.3}_{-0.1}$	$1.02^{+0.05}_{-0.1}$
M4MA2	$4.02^{+0.2}_{-0.3}$	$0.846^{+0.04}_{-0.02}$	$2.01^{+0.08}_{-0.1}$	7.09	$125.0^{+1.0}_{-1.0}$	$43.4^{+2.0}_{-6.0}$	$1.93^{+0.2}_{-0.1}$	$1.49^{+0.2}_{-0.1}$
M4MA4	$4.03^{+0.2}_{-0.4}$	$0.916^{+0.02}_{-0.03}$	$4.03^{+0.2}_{-0.4}$	3.54	$109.0^{+0.2}_{-0.5}$	$20.3^{+2.0}_{-0.5}$	$2.38^{+0.1}_{-0.3}$	$2.41^{+0.1}_{-0.3}$
M4MA6	$3.97^{+0.2}_{-0.4}$	$0.959^{+0.02}_{-0.02}$	$5.96^{+0.3}_{-0.6}$	2.36	$76.3^{+0.3}_{-0.6}$	$11.7^{+0.7}_{-0.4}$	$2.94^{+0.4}_{-0.3}$	$3.29^{+0.4}_{-0.2}$
M4MA8	$4.05^{+0.08}_{-0.5}$	$0.979^{+0.02}_{-0.03}$	$8.1^{+0.2}_{-1.0}$	1.77	$68.5^{+0.6}_{-0.4}$	$8.38^{+0.3}_{-0.3}$	$3.41^{+0.3}_{-0.6}$	$4.15^{+0.4}_{-1.0}$
M4MA10	$3.91^{+0.2}_{-0.2}$	$0.994^{+0.03}_{-0.01}$	$9.78^{+0.5}_{-0.6}$	1.42	$59.7^{+0.2}_{-0.2}$	$6.27^{+0.2}_{-0.3}$	$3.69^{+0.3}_{-0.1}$	$4.23^{+0.9}_{-0.3}$
M4MA100	$4.21^{+0.2}_{-0.08}$	$1.02^{+0.03}_{-0.02}$	$105.0^{+5.0}_{-2.0}$	0.142	$6.29^{+0.4}_{-0.4}$	$0.203^{+0.01}_{-0.01}$	$21.0^{+3.0}_{-2.0}$	$24.2^{+5.0}_{-2.0}$
M4MA1000	$4.31^{+0.1}_{-0.2}$	$1.05^{+0.02}_{-0.01}$	$1080.0^{+30.0}_{-50.0}$	0.0142	$0.391^{+0.4}_{-0.3}$	$0.00519^{+0.001}_{-0.001}$	$115.0^{+20.0}_{-40.0}$	$128.0^{+30.0}_{-50.0}$
M6MA01	$6.96^{+0.5}_{-0.8}$	$1.35^{+0.05}_{-0.04}$	$0.116^{+0.008}_{-0.01}$	213.0	$3.86^{+0.3}_{-0.7}$	$325.0^{+20.0}_{-60.0}$	$29.0^{+4.0}_{-3.0}$	$0.115^{+0.008}_{-0.01}$
M6MA05	$6.44^{+0.2}_{-0.1}$	$1.21^{+0.02}_{-0.04}$	$0.536^{+0.02}_{-0.01}$	42.5	$58.0^{+1.0}_{-0.7}$	$169.0^{+10.0}_{-10.0}$	$5.02^{+0.3}_{-0.3}$	$0.535^{+0.01}_{-0.01}$
M6MA1	$6.01^{+0.8}_{-0.8}$	$0.844^{+0.04}_{-0.02}$	$1.0^{+0.1}_{-0.1}$	21.3	$157.0^{+1.0}_{-4.0}$	$121.0^{+10.0}_{-20.0}$	$2.73^{+0.2}_{-0.2}$	$0.937^{+0.1}_{-0.2}$
M6MA2	$5.81^{+0.3}_{-0.3}$	$0.844^{+0.03}_{-0.03}$	$1.94^{+0.1}_{-0.09}$	10.6	$217.0^{+2.0}_{-0.5}$	$83.7^{+9.0}_{-5.0}$	$2.1^{+0.2}_{-0.1}$	$1.58^{+0.09}_{-0.09}$
M6MA4	$6.23^{+0.1}_{-0.4}$	$0.94^{+0.02}_{-0.01}$	$4.15^{+0.08}_{-0.3}$	5.32	$202.0^{+0.8}_{-2.0}$	$42.8^{+2.0}_{-5.0}$	$2.55^{+0.2}_{-0.2}$	$2.53^{+0.3}_{-0.2}$
M6MA6	$5.96^{+0.4}_{-0.6}$	$0.946^{+0.02}_{-0.01}$	$5.96^{+0.4}_{-0.6}$	3.54	$168.0^{+1.0}_{-1.0}$	$25.8^{+3.0}_{-2.0}$	$2.82^{+0.3}_{-0.2}$	$3.04^{+0.3}_{-0.2}$
M6MA8	$5.96^{+0.2}_{-0.5}$	$0.979^{+0.01}_{-0.01}$	$7.95^{+0.2}_{-0.6}$	2.66	$139.0^{+0.3}_{-0.9}$	$17.4^{+1.0}_{-0.6}$	$3.39^{+0.2}_{-0.4}$	$3.73^{+0.2}_{-0.4}$
M6MA10	$5.99^{+0.2}_{-0.5}$	$0.99^{+0.02}_{-0.02}$	$9.99^{+0.4}_{-0.8}$	2.13	$124.0^{+0.5}_{-1.0}$	$12.6^{+1.0}_{-0.4}$	$3.82^{+0.8}_{-0.6}$	$4.11^{+1.0}_{-0.7}$
M8MA01	$8.7^{+0.09}_{-0.9}$	$1.49^{+0.02}_{-0.1}$	$0.109^{+0.001}_{-0.01}$	284.0	$4.53^{+0.4}_{-0.7}$	$488.0^{+40.0}_{-90.0}$	$32.0^{+4.0}_{-4.0}$	$0.108^{+0.001}_{-0.01}$
M8MA05	$8.35^{+0.2}_{-0.3}$	$1.14^{+0.02}_{-0.02}$	$0.522^{+0.01}_{-0.02}$	56.7	$90.2^{+1.0}_{-0.6}$	$278.0^{+20.0}_{-30.0}$	$5.01^{+0.3}_{-0.4}$	$0.505^{+0.01}_{-0.03}$
M8MA1	$8.16^{+0.6}_{-1.0}$	$0.837^{+0.04}_{-0.03}$	$1.02^{+0.08}_{-0.1}$	28.4	$257.0^{+2.0}_{-4.0}$	$205.0^{+10.0}_{-20.0}$	$2.74^{+0.3}_{-0.3}$	$0.92^{+0.07}_{-0.1}$
M8MA2	$8.15^{+0.4}_{-0.5}$	$0.863^{+0.03}_{-0.03}$	$2.04^{+0.1}_{-0.1}$	14.2	$395.0^{+1.0}_{-1.0}$	$148.0^{+7.0}_{-8.0}$	$2.25^{+0.2}_{-0.2}$	$1.59^{+0.1}_{-0.2}$
M8MA4	$7.99^{+0.3}_{-0.4}$	$0.933^{+0.01}_{-0.03}$	$4.0^{+0.1}_{-0.2}$	7.09	$344.0^{+0.8}_{-2.0}$	$72.7^{+4.0}_{-8.0}$	$2.41^{+0.2}_{-0.1}$	$2.3^{+0.2}_{-0.2}$
M8MA6	$7.97^{+0.4}_{-0.9}$	$0.938^{+0.02}_{-0.02}$	$5.98^{+0.3}_{-0.7}$	4.73	$278.0^{+2.0}_{-1.0}$	$42.4^{+7.0}_{-1.0}$	$2.84^{+0.2}_{-0.5}$	$2.93^{+0.3}_{-0.6}$
M8MA8	$7.82^{+0.4}_{-0.4}$	$0.994^{+0.01}_{-0.02}$	$7.82^{+0.4}_{-0.4}$	3.54	$247.0^{+0.8}_{-1.0}$	$31.5^{+2.0}_{-2.0}$	$3.2^{+0.2}_{-0.3}$	$3.46^{+0.5}_{-0.3}$
M8MA10	$8.06^{+0.2}_{-1.0}$	$1.01^{+0.02}_{-0.03}$	$10.1^{+0.3}_{-1.0}$	2.84	$197.0^{+1.0}_{-0.5}$	$22.3^{+1.0}_{-0.5}$	$3.72^{+0.6}_{-0.4}$	$3.89^{+0.6}_{-0.5}$

Table 1 – *continued*

	Turbulence		Large-scale $\boldsymbol{B}$-field		Fluctuating $\boldsymbol{B}$-field			Total $\boldsymbol{B}$-field
Simulation ID	$\mathcal{M}$	$\frac{\ell_{\mathrm{cor},v}}{\ell_0}$	$\mathcal{M}_{\mathrm{A0}}$	$\frac{B_0}{c_{\mathrm{s}}\rho_0^{1/2}}$	$\left\langle \frac{\delta B^2}{c_{\mathrm{s}}^2\rho_0} \right\rangle_{\mathcal{V}}$	$\left\langle \left(\frac{\delta \boldsymbol{B}\cdot\boldsymbol{B}_0}{c_{\mathrm{s}}^2\rho_0} \right)^2 \right\rangle_{\mathcal{V}}^{1/2}$	$\mathcal{M}_{\mathrm{A,turb}}$	$\mathcal{M}_{\mathrm{A,total}}$
(1)	(2)	(3)	(4)	(5)	(6)	(7)	(8)	(9)
M10MA01	$11.3^{+0.3}_{-1.0}$	$1.45^{+0.07}_{-0.09}$	$0.113^{+0.003}_{-0.01}$	354.0	$6.76^{+1.0}_{-1.0}$	$720.0^{+100.0}_{-200.0}$	$33.7^{+8.0}_{-7.0}$	$0.112^{+0.003}_{-0.01}$
M10MA05	$10.2^{+0.3}_{-0.3}$	$1.13^{+0.02}_{-0.02}$	$0.509^{+0.01}_{-0.02}$	70.9	$143.0^{+2.0}_{-2.0}$	$420.0^{+20.0}_{-40.0}$	$4.88^{+0.6}_{-0.5}$	$0.496^{+0.02}_{-0.02}$
M10MA1	$9.72^{+0.9}_{-0.9}$	$0.868^{+0.03}_{-0.03}$	$0.972^{+0.09}_{-0.09}$	35.4	$338.0^{+3.0}_{-4.0}$	$309.0^{+20.0}_{-40.0}$	$2.79^{+0.4}_{-0.1}$	$0.888^{+0.06}_{-0.1}$
M10MA2	$10.5^{+0.3}_{-0.8}$	$0.888^{+0.02}_{-0.02}$	$2.1^{+0.07}_{-0.2}$	17.7	$549.0^{+0.9}_{-1.0}$	$215.0^{+9.0}_{-10.0}$	$2.39^{+0.1}_{-0.3}$	$1.56^{+0.2}_{-0.1}$
M10MA4	$10.3^{+0.4}_{-0.4}$	$0.931^{+0.03}_{-0.03}$	$4.12^{+0.2}_{-0.2}$	8.86	$529.0^{+2.0}_{-2.0}$	$112.0^{+8.0}_{-6.0}$	$2.42^{+0.4}_{-0.2}$	$2.32^{+0.4}_{-0.2}$
M10MA6	$9.78^{+0.3}_{-1.0}$	$0.952^{+0.02}_{-0.03}$	$5.87^{+0.2}_{-0.7}$	5.91	$398.0^{+2.0}_{-0.7}$	$65.2^{+7.0}_{-3.0}$	$2.7^{+0.3}_{-0.4}$	$2.77^{+0.3}_{-0.4}$
M10MA8	$10.0^{+0.4}_{-0.9}$	$0.997^{+0.02}_{-0.02}$	$8.03^{+0.3}_{-0.7}$	4.43	$346.0^{+1.0}_{-1.0}$	$46.7^{+4.0}_{-1.0}$	$3.27^{+0.4}_{-0.4}$	$3.41^{+0.4}_{-0.6}$
M10MA10	$9.42^{+0.2}_{-0.5}$	$0.99^{+0.01}_{-0.01}$	$9.42^{+0.2}_{-0.5}$	3.54	$288.0^{+2.0}_{-3.0}$	$34.3^{+3.0}_{-4.0}$	$3.37^{+0.3}_{-0.2}$	$3.5^{+0.5}_{-0.3}$

Note. All simulations listed are run with grid resolutions of 16^3, 36^3, 72^3, 144^3, and 288^3. All statistics are spatially averaged over the entire domain, $\mathcal{V} = \mathcal{V}_L$, and are computed for 51 time realizations, across five correlation times of the Ornstein–Uhlenbeck forcing function. From the distributions in time, we report the values for the 16th, 50th, and 84th percentiles. This process minimizes the possibility of using statistics that are undergoing temporally intermittent turbulent events (Beattie et al. 2021b). Column (1): the simulation ID, used throughout this study. Column (2): the turbulent Mach number, $\mathcal{M} \equiv \langle (\delta v/c_{\mathrm{s}})^2 \rangle_{\mathcal{V}_L}^{1/2}$. Column (3): the correlation scale of the turbulence, $\ell_{\mathrm{cor},\,v}$, in units of the driving scale, ℓ_0, defined directly from the power spectra in equation (32). Column (4): the Alfvén Mach number of the mean magnetic field, $\mathcal{M}_{\mathrm{A0}} \equiv \langle (\delta v \sqrt{4\pi\rho_0})/B_0 \rangle$, with fluctuations coming from δv, since $\partial_{x_i} \boldsymbol{B}_0 = \partial_t \boldsymbol{B}_0 = 0$. Column (5): the mean magnetic field strength in units of $c_{\mathrm{s}}\rho_0^{1/2}$. Column (6): the volume-averaged square of the turbulent magnetic field, proportional to the turbulent magnetic energy, in units of thermal energy. Column (7): the volume-averaged root-mean-squared (rms) of the magnetic coupling term $\delta\boldsymbol{B}\cdot\boldsymbol{B}_0$, in units of thermal energy. Column (8): the Alfvén Mach number of the turbulent magnetic field, equation (28). Column (9): the Alfvén Mach number of the total magnetic field, equation (29).

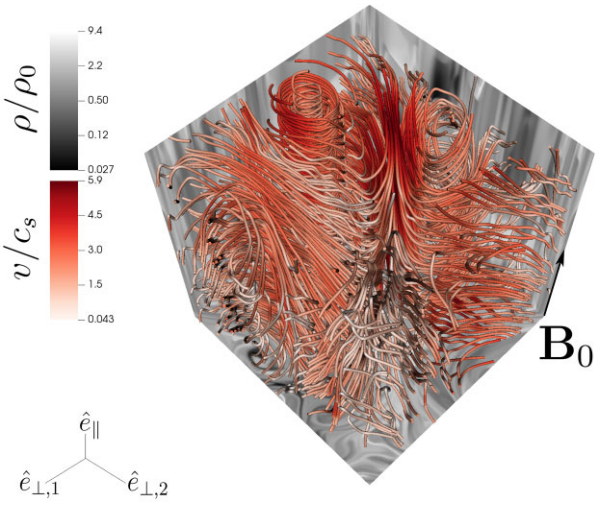

Figure 1. Typical velocity (red) streamline structure in sub-Alfvénic mean-field turbulence, with $\mathcal{M} = 2$ and $\mathcal{M}_{\mathrm{A0}} = 0.1$. The direction of the mean field, $\boldsymbol{B}_0$, is shown in the bottom right-hand corner of the box. Slices of the density are shown in grey scale at the box edges. Ordered vortex structures occupy the full extent of the box along $\hat{e}_\parallel$, and out to the driving scale in $\hat{e}_\perp$.

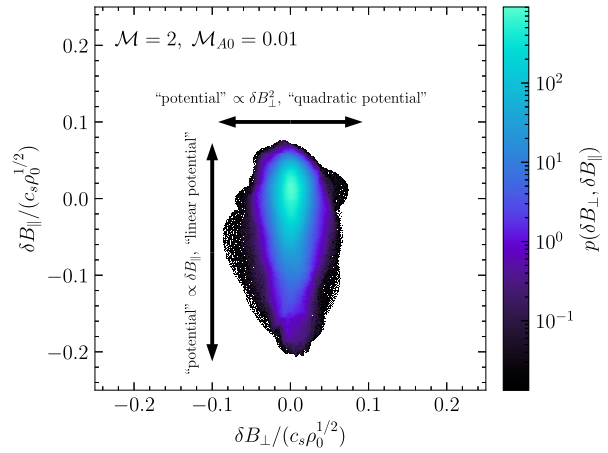

Figure 2. The joint probability density function (PDF) for $\delta B_\parallel$ and $\delta B_\perp$ for the M2MA001 simulation, showing a long, asymmetric tail into the negative values for $\delta B_\parallel$. As demonstrated in S+2021, the $\delta B_\perp$ fluctuations are symmetric about $\delta B_\perp = 0$, and are analogous to a harmonic oscillator (in magnetic amplitude space) that is restored by the magnetic tension $\propto \delta B_\perp^2$ with a quadratic potential. On the other hand, the $\delta B_\parallel$ amplitude fluctuates anharmonically, $\propto \delta B_\parallel$, with a linear potential. In sub-to-trans-Alfvénic compressible MHD the anharmonic, parallel magnetic field fluctuations contain most of the magnetic energy.

The dimensionless turbulent kinetic energy, normalized by the mean thermal pressure (similarly to e_{mag}; see equation 5), is

$$e_{\mathrm{kin}} = \frac{1}{2}\left(\frac{\delta v}{c_{\mathrm{s}}}\right)^2, \tag{6}$$

which acts as an energy reservoir for the magnetic field fluctuations via the velocity term in the induction equation, equation (3). Considering our ideal, isothermal (in our units, the thermal energy is $e_{\mathrm{thermal}} = 3/2$), MHD system, the total energy is then

$$e_{\mathrm{tot}} = \frac{1}{2}\left(\frac{\delta v}{c_{\mathrm{s}}}\right)^2 + \frac{1}{8\pi c_{\mathrm{s}}^2\rho_0}\left(B_0^2 + 2\delta\boldsymbol{B}\cdot\boldsymbol{B}_0 + \delta B^2\right) + \frac{3}{2}, \tag{7}$$

and for just the 'total' turbulent energy,

$$e_{\mathrm{turb}} = \frac{1}{2}\left(\frac{\delta v}{c_{\mathrm{s}}}\right)^2 + \frac{1}{8\pi c_{\mathrm{s}}^2\rho_0}\left(2\delta\boldsymbol{B}\cdot\boldsymbol{B}_0 + \delta B^2\right), \tag{8}$$

where only the δB^2 and $\delta\boldsymbol{B}\cdot\boldsymbol{B}_0$ terms are retained in the magnetic energy, because they contain the turbulent contribution.

In a fluid with initially weak magnetic fluctuations and $B_0 = 0$, e_{kin} (equation 6) will transfer energy and enhance e_{mag} (equation 5 with B_0 set to 0) via the small-scale turbulent dynamo (for a recent review see McKee et al. 2020). A standard ansatz of dynamo theory

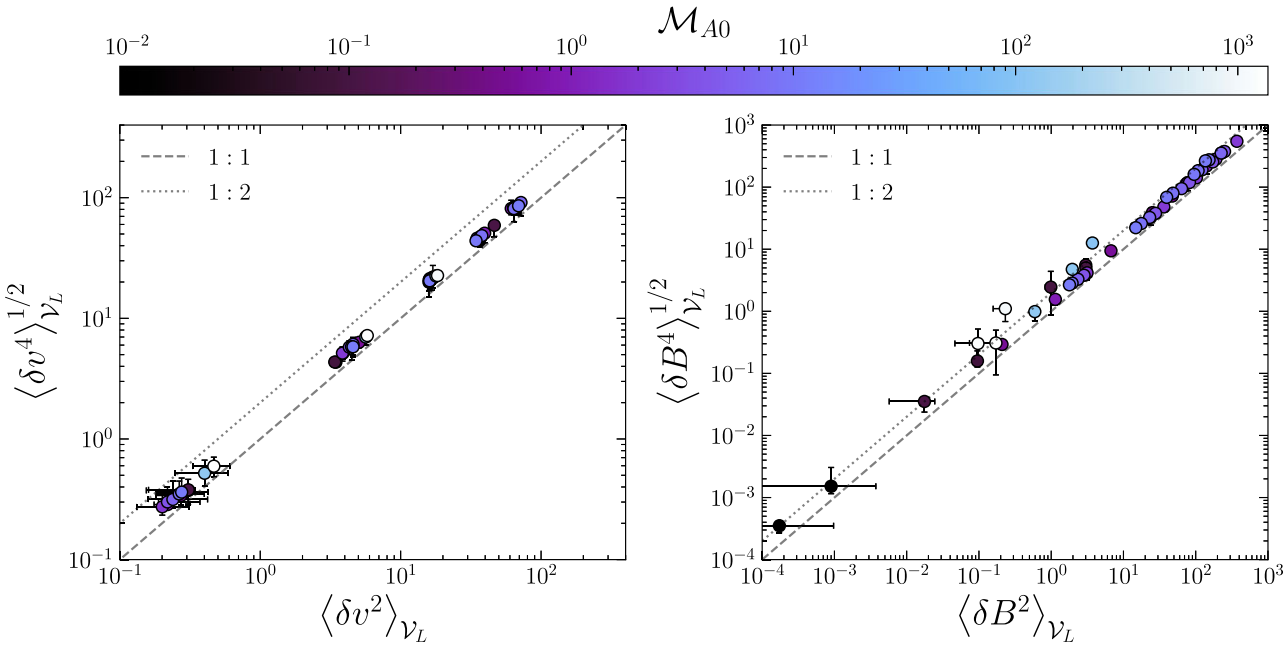

Figure 3. The square root of the fourth-order turbulent velocity (left) and magnetic field (right) moments as a function of second-order moments, coloured by $\mathcal{M}_{A0}$, for all of the simulations listed in Table 1. The second-order moments of the turbulent fields are approximately equivalent to the scaled fourth-order moments, $\langle \delta v^4 \rangle_{\mathcal{V}}^{1/2} = (1.3 \pm 0.3) \langle \delta v^2 \rangle_{\mathcal{V}}$, and $\langle \delta B^4 \rangle_{\mathcal{V}}^{1/2} = (1.5 \pm 0.4) \langle \delta B^2 \rangle_{\mathcal{V}}$, rarely deviating by more than a factor of 2 (dotted line) from the 1:1 dashed line. This means that the standard deviation of the magnetic and kinetic energy distributions scale with the mean.

is that saturation will be reached between the turbulent fields, such that

$$\frac{\langle e_{\rm mag} \rangle_{\mathcal{V}}}{\langle e_{\rm kin} \rangle_{\mathcal{V}}} = \alpha_{\rm sat}, \tag{9}$$

where $0 \leq \alpha_{\rm sat} \leq 1$. The value of $\alpha_{\rm sat}$ is a function of $\mathcal{M}$, the Alfvén Mach number $\mathcal{M}_{\rm A}$ (a precise definition for which we defer to Section 5), the nature of the driving mechanism, $\boldsymbol{f}$, in particular if it is compressive $\nabla \times \boldsymbol{f} = 0$ or solenoidal $\nabla \cdot \boldsymbol{f} = 0$, and the Prandtl and Reynolds numbers of the fluid (Federrath et al. 2011a, 2014; Schober et al. 2012, 2015; Federrath 2016; Achikanath Chirakkara et al. 2021; Kriel et al. 2022). The exact physics of the saturation is still an open problem in dynamo theory, but most likely the saturation develops due to the effect of strong magnetic fields on both the amplification (via field line stretching), diffusion of magnetic fields and instabilities caused by tearing and magnetic reconnection (Schekochihin et al. 2002; Xu & Lazarian 2016; Seta & Federrath 2021a; Galishnikova, Kunz & Schekochihin 2022); however, the exact value of $\alpha_{\rm sat}$ and its dependence on other parameters is not important for our purposes. What is significant is that, assuming that the energy transfer from $e_{\rm kin}$ to $e_{\rm mag}$ is solely through the turbulent components of the respective fields, including the turbulent and large-scale field coupling term for the more general case where $B_0 \neq 0$, from equations (8) and (9) becomes

$$\frac{1}{8\pi c_{\rm s}^2 \rho_0} \left\langle 2\delta \boldsymbol{B} \cdot \boldsymbol{B}_0 + \delta B^2 \right\rangle_{\mathcal{V}} = \frac{\alpha_{\rm sat}}{2} \left\langle \left(\frac{\delta v}{c_{\rm s}} \right)^2 \right\rangle_{\mathcal{V}}, \tag{10}$$

which naively reduces to

$$\frac{1}{8\pi c_{\rm s}^2 \rho_0} \left\langle \delta B^2 \right\rangle_{\mathcal{V}} = \frac{\alpha_{\rm sat}}{2} \left\langle \left(\frac{\delta v}{c_{\rm s}} \right)^2 \right\rangle_{\mathcal{V}}, \tag{11}$$

if $\langle \delta \boldsymbol{B} \cdot \boldsymbol{B}_0 \rangle_{\mathcal{V}} = \langle \delta B_{\parallel} \rangle_{\mathcal{V}} B_0 = 0$ because $\langle \delta B_{\parallel} \rangle_{\mathcal{V}} = 0$ when $\mathcal{V}$ captures a few correlation lengths of the turbulence, for the regular Reynolds (1895) decomposition of a stochastic field.[7] But this is not necessarily a sensible result because when the large-scale field is strong the coupling term is leading order in the turbulent magnetic energy, and all energy reservoirs should be strictly positive. Because the coupling term is the only term that is not positive semidefinite in equation (10) we may want to treat averaging the equation with more care.

These considerations lead us to consider an alternative ansatz, one that enforces the positivity of all terms. Our approach is to take the second-moments of equation (10), but also taking the square root to ensure that the units are appropriate for an energy balance,

$$\frac{1}{8\pi c_{\rm s}^2 \rho_0} \left\langle \left(2\delta \boldsymbol{B} \cdot \boldsymbol{B}_0 + \delta B^2 \right)^2 \right\rangle_{\mathcal{V}}^{1/2} = \frac{\alpha_{\rm sat}}{2} \left\langle \left(\frac{\delta v}{c_{\rm s}} \right)^4 \right\rangle_{\mathcal{V}}^{1/2}. \tag{12}$$

The physical interpretation of this balance is that instead of balancing the means of the energy distributions, we balance the root-mean-squared (rms) values, which are a measure of the typical local fluctuations in energy of the plasma. This method of volume-averaging equation (10) gives rise to fourth-order terms in velocity and magnetic field fluctuations (second order in energies). Note that for finite $\mathcal{M}_{A0}$, $\alpha_{\rm sat}$ is now different from $\alpha_{\rm sat}$ in small-scale dynamo experiments (where $B_0 = 0$) because it is now sensitive to the large-scale field through the energy contribution of the coupling term.

To better understand the fourth-order terms we plot them as a function of second-order terms in Fig. 3 and show the 1:1 and 1:2 lines with dashes and dots, in each of the plots, respectively. Using

[7] S+2021 showed that even this leads to complications because $\delta \boldsymbol{B} \cdot \boldsymbol{B}_0$ is analogous to a potential energy, which does not make sense to average because it is invariant to gauge transforms, not positive definite, nor symmetric around the minimum energy state for $\delta B_{\parallel}$. See discussion in section 4 of S+2021 for more details.

least-squares fitting we find that $\langle \delta v^4 \rangle_{\mathcal{V}}^{1/2} = (1.3 \pm 0.3) \langle \delta v^2 \rangle_{\mathcal{V}}$, and $\langle \delta B^4 \rangle_{\mathcal{V}}^{1/2} = (1.5 \pm 0.4) \langle \delta B^2 \rangle_{\mathcal{V}}$, hence, within $\approx 1\sigma$, the proportionality constants are approximately unity. Physically, this means that as the mean of the energy distributions increase, so does the rms, or spread of the distributions. This has been shown before, for example, in Schekochihin et al. (2004), where they found $\langle \delta B^4 \rangle_{\mathcal{V}}^{1/2} \approx \sqrt{2} \langle \delta B^2 \rangle_{\mathcal{V}}$ (see fig. 11, saturated regime). This is an important point, because it means that the contributions from the turbulent fields remain approximately the same in both averaging schemes, equations (10) and (12), but now we are able to properly include the energy contribution from the coupling term.

3.2 Weak and strong *B*-field limits for rms energy balance

Consider now equation (12) in the weak $\boldsymbol{B}_0$ regime, such that $B_0 \ll \delta B$, averaged over $\mathcal{V}$. This means

$$\left\langle \left(2\delta B \cdot B_0 + \delta B^2\right)^2 \right\rangle_{\mathcal{V}} = \left\langle (2\delta \boldsymbol{B} \cdot B_0)^2 \right\rangle_{\mathcal{V}} + \left\langle 4(\delta \boldsymbol{B} \cdot \boldsymbol{B}_0)\delta B^2 \right\rangle_{\mathcal{V}} + \left\langle \delta B^4 \right\rangle_{\mathcal{V}} \tag{13}$$

$$\sim \left\langle \delta B^4 \right\rangle_{\mathcal{V}}, \tag{14}$$

to leading δB^4 order, and therefore

$$\frac{\langle \delta B^4 \rangle_{\mathcal{V}}^{1/2}}{8\pi c_s^2 \rho_0} \approx \frac{\alpha_{\rm sat}}{2} \left\langle \left(\frac{\delta v}{c_s}\right)^4 \right\rangle_{\mathcal{V}}^{1/2}. \tag{15}$$

Based upon our numerical results this equation can be rewritten in terms of second-order terms (see Fig. 3),

$$\frac{\langle \delta B^2 \rangle_{\mathcal{V}}}{8\pi c_s^2 \rho_0} \approx \frac{\alpha_{\rm sat}}{2} \left\langle \left(\frac{\delta v}{c_s}\right)^2 \right\rangle_{\mathcal{V}}, \tag{16}$$

with the $\langle \delta B^2 \rangle_{\mathcal{V}}$ dominating the balance between the kinetic turbulent energy. Likewise, as Federrath (2016) framed the relation, the kinetic energy is feeding the magnetic field through the δB^2 term in this regime.

In the strong $\boldsymbol{B}_0$ regime we have $B_0 \gg \delta B$, and hence, to leading B_0^2 order equation (13) becomes

$$\left\langle \left(2\delta \boldsymbol{B} \cdot \boldsymbol{B}_0 + \delta B^2\right)^2 \right\rangle_{\mathcal{V}} \sim 2 \left\langle (\delta \boldsymbol{B} \cdot \boldsymbol{B}_0)^2 \right\rangle_{\mathcal{V}}, \tag{17}$$

with the $2\langle (\delta \boldsymbol{B} \cdot \boldsymbol{B}_0)^2 \rangle_{\mathcal{V}}^{1/2}$ term dominating the balance. Hence the energy balance must be between

$$\frac{\langle (\delta \boldsymbol{B} \cdot \boldsymbol{B}_0)^2 \rangle_{\mathcal{V}}^{1/2}}{4\pi c_s^2 \rho_0} \approx \frac{\alpha_{\rm sat}}{2} \left\langle \left(\frac{\delta v}{c_s}\right)^4 \right\rangle_{\mathcal{V}}^{1/2}, \tag{18}$$

which we can similarly reduce to second-order terms,

$$\frac{\langle (\delta \boldsymbol{B} \cdot \boldsymbol{B}_0)^2 \rangle_{\mathcal{V}}^{1/2}}{4\pi c_s^2 \rho_0} \approx \frac{\alpha_{\rm sat}}{2} \left\langle \left(\frac{\delta v}{c_s}\right)^2 \right\rangle_{\mathcal{V}}. \tag{19}$$

Note now this is the same relation derived in S+2021, but it comes from directly considering the rms balanced energy equations, and then invoking the numerical result that the square root of the fourth-order velocity and magnetic terms scale almost perfectly with the second-order terms. The second–fourth moment relation should be accurate to a factor less than 2, as indicated in Fig. 3. Establishing the strong mathematical footing for this relation is a key result from our study.

We will return to equation (10) and the two limiting cases, equations (16) and (19), throughout this study. Specifically, we will show that by using this simple energy balance model that includes $\langle (\delta \boldsymbol{B} \cdot \boldsymbol{B}_0)^2 \rangle_{\mathcal{V}}^{1/2}$, we can learn a great deal about the magnetic and velocity field fluctuations. First, we start by understanding the nature of the coupling term.

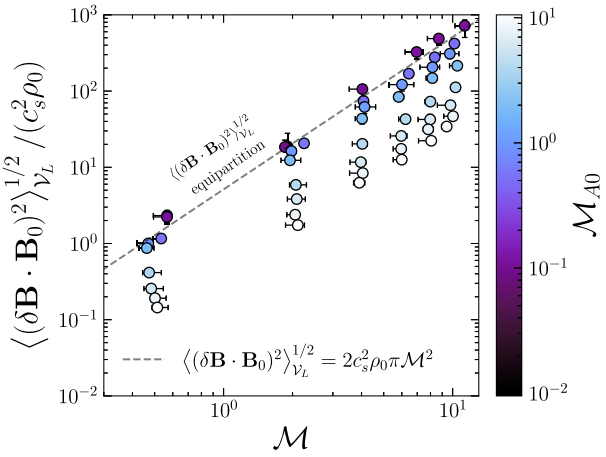

Figure 4. The magnetic coupling term, $\langle (\delta \boldsymbol{B} \cdot \boldsymbol{B}_0)^2 \rangle_{\mathcal{V}}^{1/2}$, as a function of the $\mathcal{M}$, coloured by $\mathcal{M}_{\rm A0}$, for all of the simulations up to $\mathcal{M}_{\rm A0} = 10$. We show the strong-field model, equation (20), for the coupling term, indicated with the grey dashed line, which is valid for the simulations with dark shading, assuming exact energy equipartition between the turbulent kinetic and the coupling term energy.

4 MODELS FOR $\langle (\delta \boldsymbol{B} \cdot \boldsymbol{B}_0)^2 \rangle_{\mathcal{V}}^{1/2}$

4.1 Strong mean field, $B_0 \gg \delta B$

Assuming that the kinetic energy fluctuations are in energy equipartition with the coupling term ($\alpha_{\rm sat} = 1$) it immediately follows from equation (19) that in the strong-mean-field regime the coupling term is

$$\langle (\delta \boldsymbol{B} \cdot \boldsymbol{B}_0)^2 \rangle_{\mathcal{V}}^{1/2} = 2 c_s^2 \rho_0 \pi \mathcal{M}^2. \tag{20}$$

We plot this predicted relationship, along with the values measured from our simulations, in Fig. 4. The plot is consistent with our expectations: simulations in the strong-mean-field regime, $\mathcal{M}_{\rm A0} < 1$, sit very close to the equipartition line, while those with $\mathcal{M}_{\rm A0} > 1$ sit below it, indicating that the $\langle \delta B^2 \rangle_{\mathcal{V}}$ term is playing an increasingly large role in the energy balance as we transition to the weak-mean-field regime.

Even in the strong-mean-field regime, we see weak variation with $\mathcal{M}$ in how closely the simulations follow the prediction of equation (20). For low $\mathcal{M}$, the strong-field model works best, but as $\mathcal{M}$ gets larger there is some scatter to lower values of $\langle (\delta \boldsymbol{B} \cdot \boldsymbol{B}_0)^2 \rangle_{\mathcal{V}}^{1/2}$, even in the sub-Alfvénic simulations. This suggests that for $\mathcal{M}_{\rm A0} \gtrsim 1$ there are some contributions to the magnetic energy through the $\langle \delta B^2 \rangle_{\mathcal{V}}$ term, which we neglect in our model, i.e. the shear Alfvén waves and fast modes that perturb the magnetic field perpendicular to $\boldsymbol{B}_0$. Of course, the turbulence naturally excites such modes but it is plausible that the magnetic tension significantly suppresses them when $B_0/\delta B$ is large.

To further quantify when each of the magnetic terms in equation (12) contributes the most to the energy balance we examine the ratio of the two magnetic energy reservoir terms, $\langle (\delta \boldsymbol{B} \cdot \boldsymbol{B}_0)^2 \rangle_{\mathcal{V}}^{1/2} / \langle \delta B^2 \rangle_{\mathcal{V}}$. We estimate $\langle \delta B^2 \rangle_{\mathcal{V}}$ following the fluc-

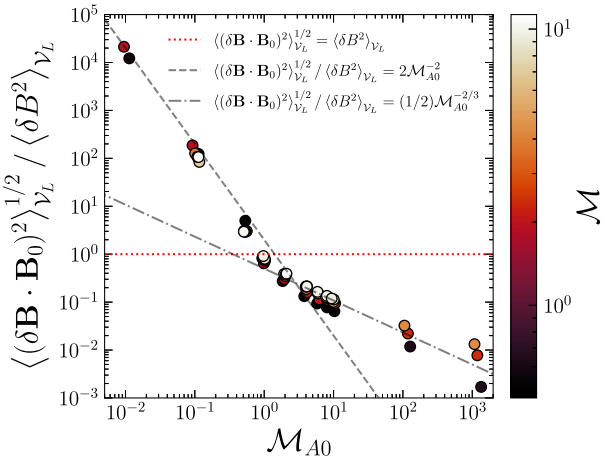

Figure 5. The ratio of the magnetic coupling term, $\langle(\delta\boldsymbol{B}\cdot\boldsymbol{B}_0)^2\rangle_{\mathcal{V}}^{1/2}$, to the turbulent magnetic energy, $\langle\delta B^2\rangle_{\mathcal{V}}$ as a function of $\mathcal{M}_{A0}$, coloured by the $\mathcal{M}$, for all simulations. We show in red dots the equipartition between the two terms. The grey dashed line shows the strong-field model, equation (22), which is valid for $B_0 \gg \delta B$, or $\mathcal{M}_{A0} \lesssim 2$, and the grey dot–dashed line for the weak-field model, equation (25), valid for $\mathcal{M}_{A0} > 2$.

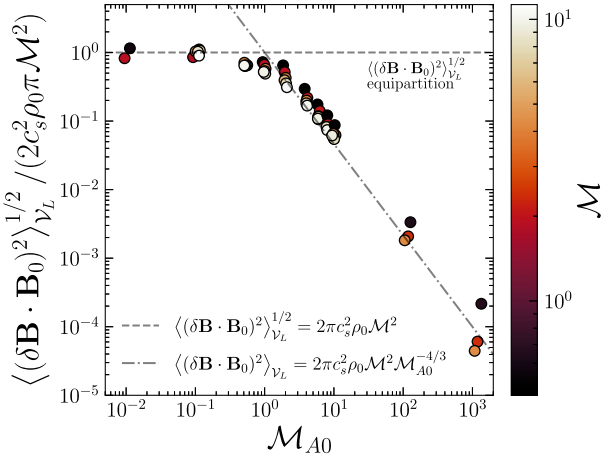

Figure 6. The magnetic coupling term, $\langle(\delta\boldsymbol{B}\cdot\boldsymbol{B}_0)^2\rangle_{\mathcal{V}}^{1/2}$, compensated by equation (20), as a function $\mathcal{M}_{A0}$, coloured by $\mathcal{M}$, for all simulations. This choice of compensation reveals the $\mathcal{M}_{A0}$ dependency in the super-Alfvénic turbulence regime, which we provide a model for in Section 4.2, shown with the grey dot–dashed line.

tuation models in Federrath (2016) and Beattie et al. (2020),[8] which leads to a predicted relationship

$$\langle\delta B^2\rangle_{\mathcal{V}}^{1/2} = c_s\sqrt{\pi\rho_0}\mathcal{M}\mathcal{M}_{A0}. \tag{21}$$

The ratio between the coupling term to the energy from the above equation squared is then

$$\frac{\langle(\delta\boldsymbol{B}\cdot\boldsymbol{B}_0)^2\rangle_{\mathcal{V}}^{1/2}}{\langle\delta B^2\rangle_{\mathcal{V}}} = \frac{2}{\mathcal{M}_{A0}^2} = 2\frac{e_{\rm mag,0}}{e_{\rm kin}}, \tag{22}$$

where $\mathcal{M}_{A0}^{-2} = e_{\rm mag,0}/e_{\rm kin}$. This means at $\mathcal{M}_{A0} = e_{\rm mag,0}/e_{\rm kin} = 1$, i.e. when the turbulent and $\boldsymbol{B}_0$ energy are in equipartition, we expect $\langle(\delta\boldsymbol{B}\cdot\boldsymbol{B}_0)^2\rangle_{\mathcal{V}}^{1/2}/\langle\delta B^2\rangle_{\mathcal{V}} = 2$. We plot the relation measured in the simulations in Fig. 5, showing our predicted scaling in the strong-mean-field regime with the dashed, grey line. Again, the plot shows excellent agreement between the model and the MHD data in the range $0.01 \leq \mathcal{M}_{A0} \leq 2$, indicating a perfect balancing act between $\langle(\delta\boldsymbol{B}\cdot\boldsymbol{B}_0)^2\rangle_{\mathcal{V}}^{1/2}$ and $\langle\delta v^2\rangle_{\mathcal{V}}$. The $\mathcal{M}_{A0} \approx 2$ transition is where $\langle\delta B^2\rangle_{\mathcal{V}}/B_0^2 \approx 1$, and the turbulent magnetic field starts to dominate the magnetic energy reservoir. We will find that this is a reoccurring transition phase for compressible MHD turbulence.

4.2 Weak large-scale field, $B_0 \lesssim \delta B$

Beyond $\mathcal{M}_{A0} \gtrsim 2$ energy balance arguments only work if the saturation level changes as a function of plasma parameters, because $\delta\boldsymbol{B}$ is not constant with $\boldsymbol{B}_0$ (Federrath 2016; Beattie et al. 2020). We have one free parameter, $\alpha_{\rm sat}$, which need not be constant for all $\mathcal{M}_{A0}$ and $\mathcal{M}$ (Federrath 2016; Achikanath Chirakkara et al. 2021; Seta & Federrath 2021a). To extract $\alpha_{\rm sat}$, we model the coupling term in the super-Alfvénic regime by starting with an empirical model that Beattie et al. (2020) found held universally for $\mathcal{M}$ in the $\mathcal{M}_{A0} \gtrsim 2$ regime, $\langle\delta B^2\rangle_{\mathcal{V}}^{1/2}/B_0 = \mathcal{M}_{A0}^{2/3}$. This provides an independent estimate of the super-Alfvénic turbulent magnetic fluctuations,

$$\langle\delta B^2\rangle_{\mathcal{V}}^{1/2} = \mathcal{M}_{A0}^{2/3}B_0 = 2c_s\sqrt{\pi\rho_0}\mathcal{M}\mathcal{M}_{A0}^{-1/3}, \tag{23}$$

and therefore, equating equation (16) with the square of equation (23), $\alpha_{\rm sat} = \mathcal{M}_{A0}^{-2/3}$, which implies that as the large-scale field becomes weaker, the turbulent magnetic field saturates to smaller and smaller values because there is less total magnetic energy, consistent with what was qualitatively found in Beattie et al. (2020). Following the same steps as in Section 4.1, additionally using $B_0/(c_s\rho_0^2) = 2\sqrt{\pi}\mathcal{M}\mathcal{M}_{A0}^{-1}$, the definition of the large-scale field Alfvén Mach number, the coupling term in the super-Alfvénic regime becomes

$$\langle(\delta\boldsymbol{B}\cdot\boldsymbol{B}_0)^2\rangle_{\mathcal{V}}^{1/2} = 2\pi c_s^2\rho_0\mathcal{M}^2\mathcal{M}_{A0}^{-4/3}, \tag{24}$$

and ratio $\langle(\delta\boldsymbol{B}\cdot\boldsymbol{B}_0)^2\rangle_{\mathcal{V}}^{1/2}/\langle\delta B^2\rangle_{\mathcal{V}}$,

$$\frac{\langle(\delta\boldsymbol{B}\cdot\boldsymbol{B}_0)^2\rangle_{\mathcal{V}}^{1/2}}{\langle\delta B^2\rangle_{\mathcal{V}}} = \frac{1}{2}\mathcal{M}_{A0}^{-2/3}. \tag{25}$$

We plot equations (24) and (25), alongside their strong-field counterparts, in Figs 5 and 6, respectively. Note that Fig. 6 shows the same information as Fig. 4, but we have normalized by equation (20) to remove the $\mathcal{M}^2$ dependency. This allows us to better observe the dependence on $\mathcal{M}_{A0}$ in the $B_0 \ll \delta B$ regime. Astonishingly, through this relatively simple analysis both of the theoretical models describe the data very well, providing excellent agreement over three orders of magnitude in $\mathcal{M}_{A0}$, with no free parameters.

4.3 Discussion and caveats

We have established that for sub-to-trans-Alfvénic turbulence, the volume-averaged turbulent kinetic energy is in *exact* energy equipartition with the rms $\delta\boldsymbol{B}\cdot\boldsymbol{B}_0$ field. Each of the models in Section 4.1 relies on this assumption ($\alpha_{\rm sat} = 1$), and without any further free parameters, with such a simple model, the agreement to the numerical data in Figs 4–6 is remarkable. The models in the super-Alfvénic regime critically rely on the empirical result from Beattie et al.

[8]Note that anisotropy in the magnetic and velocity fluctuations (decomposing to perpendicular and parallel field components) was ignored in these studies, as pointed out by S+2021, but the corrections are of order unity, which we show in Appendix B, and only become important for more sensitive calculations, which we discuss later in Section 5.

(2020), $\langle \delta B^2 \rangle_{\mathcal{V}_L}^{1/2} / B_0 = \mathcal{M}_{\rm A0}^{2/3}$, but likewise, the models for the coupling and fluctuation terms outlined in Section 4.2 are in excellent agreement with the data, again, with no free parameters.

Our results therefore strongly support the Skalidis & Tassis (2021) and S+2021 model for relating the balanced rms magnetic field coupling term to the volume-averaged turbulent kinetic energy (the energy balance arguments). We hope that our treatment satisfies other authors' concerns about the Skalidis & Tassis (2021) coupling term method. These concerns have taken two forms. One is that the energy contribution from $\langle \delta \boldsymbol{B} \cdot \boldsymbol{B}_0 \rangle_{\mathcal{V}} \stackrel{\rm must}{=} 0$ because $\langle \delta \boldsymbol{B} \rangle_{\mathcal{V}} = 0$, as highlighted in the appendix of Li et al. (2022). But as has been extensively discussed in S+2021, and in Section 3 of this study, $\langle \delta \boldsymbol{B} \cdot \boldsymbol{B}_0 \rangle_{\mathcal{V}} = 0$ is not a valid way of understanding the contribution from the coupling term. The other concern raised in the appendix of Li et al. (2022) is that energy balance only involves second-order quantities; this approach by definition omits the coupling term contribution, which is first order, in the energetics. Omission of the coupling term leads to significantly underestimating the magnetic energy in sub-Alfvénic turbulence;[9] this is strongly supported by our numerical results in Figs 5 and 6. In the same figures we show that second-order terms become significant only in super-Alfvénic turbulence. Therefore, one should clearly state the magnetization level of turbulence (sub- or super-Alfvénic) before arguing about the relative contribution of the various terms in the energy balance.

Liu, Qiu & Zhang (2022) further argue that self-gravity may modify this energy balance. We do not include gravity in this study, but it is possible that gravity may collapse locally bound (by self-gravity) regions in the ISM, enhancing and creating strong magnetic fields (Sur et al. 2010). This may make the coupling term even more relevant as the regions collapse, forming convergent flows parallel to the field lines, and strengthening the magnetic field and hence the local effect of $\delta \boldsymbol{B} \cdot \boldsymbol{B}_0$. This is speculative, and the exact effects of gravity are unclear; we will return to this topic in future work. Of course, all of this work is done in the isothermal context, so our relations are only relevant to individual phases of the ISM, which are well approximated by an isothermal equation of state (e.g. Wolfire et al. 1995).

5 THE THREE ALFVÉN MACH NUMBERS

5.1 Definitions and results

The Alfvén Mach number, $\mathcal{M}_{\rm A}$, is another part of the energy balance story, because the quantity itself is directly related to the energy equilibrium in the plasma,

$$\mathcal{M}_{\rm A}^{-2} = \left\langle \frac{B^2/(8\pi)}{(1/2)\rho \delta v^2} \right\rangle_{\mathcal{V}} = \left\langle \frac{e_{\rm mag}}{e_{\rm kin}} \right\rangle_{\mathcal{V}}, \tag{26}$$

which is similar to $\alpha_{\rm sat}$ in equation (9), but not exactly the same, because $\langle X/Y \rangle_{\mathcal{V}} \neq \langle X \rangle_{\mathcal{V}} / \langle Y \rangle_{\mathcal{V}}$ if there are any correlations between X and Y, as is the case for the magnetic and kinetic energy ($\alpha_{\rm sat} = \mathcal{M}_{\rm A0}^{-2/3}$, Section 4.2).

Throughout the previous section, we utilized $\mathcal{M}_{\rm A0}$ to construct our models around values of $\boldsymbol{B}_0$. We could do this easily because $\mathcal{M}_{\rm A0}$ is an input (or at least controlled, albeit with some small variation due to velocity fluctuations) in our simulations. However, in many astrophysical turbulence studies, authors prefer to use $\mathcal{M}_{\rm A}$. For some of these studies, it is not clear if one should interpret this as the $\mathcal{M}_{\rm A}$ with respect to just turbulent fluctuations, or the total field strength. The difference between these quantities is rarely appreciated, so we make a point by defining and relating three different canonical constructions of $\mathcal{M}_{\rm A}$. The three definitions we use[10] are

$$\mathcal{M}_{\rm A0} = \left\langle \frac{\delta v \sqrt{4\pi\rho}}{B_0} \right\rangle_{\mathcal{V}}, \tag{27}$$

$$\mathcal{M}_{\rm A,turb} = \left\langle \frac{\delta v \sqrt{4\pi\rho}}{\delta B} \right\rangle_{\mathcal{V}}, \tag{28}$$

$$\mathcal{M}_{\rm A,total} = \left\langle \frac{\delta v \sqrt{4\pi\rho}}{B} \right\rangle_{\mathcal{V}}, \tag{29}$$

where the first of the three defines the large-scale field (or mean field on the system scale) Alfvén Mach number, which compares the large-scale magnetic energy with the kinetic energy, the second is the turbulent-field Alfvén Mach number, which compares the turbulent magnetic energy with the kinetic energy, and the third, the total field Alfvén Mach number.

To understand the relation between the three quantities, we plot them in Fig. 7 ($\mathcal{M}_{\rm A,total}$ in red, and $\mathcal{M}_{\rm A,turb}$ in blue, both as a function of $\mathcal{M}_{\rm A0}$). The dashed, grey line shows the one-to-one line between $\mathcal{M}_{\rm A0}$ and $\mathcal{M}_{\rm A}$. For $\mathcal{M}_{\rm A0} \lesssim 2$, $\mathcal{M}_{\rm A0} \approx \mathcal{M}_{\rm A,total}$, which means the energetics of the fluid are completely dominated by the large-scale field, and not the turbulence at all. $\mathcal{M}_{\rm A,turb}$ follows a power law in $\mathcal{M}_{\rm A0}$ that prevents the fluctuating magnetic field from ever becoming stronger than $\mathcal{M}_{\rm A,turb} \approx 2$. Once the turbulent field has reached $\mathcal{M}_{\rm A} \approx 2$, it then begins weakening again, but this time $\mathcal{M}_{\rm A,turb} \approx \mathcal{M}_{\rm A,total}$, with $\mathcal{M}_{\rm A,total} \lesssim \mathcal{M}_{\rm A0}$, i.e. transitioning into a turbulent magnetic field dominant regime as the $\boldsymbol{B}$-field becomes tangled and more energy dense than the large-scale field. As discussed in Section 4.1, the $\mathcal{M}_{\rm A0} = 2$ transition between the sub-and-super-Alfvénic regimes defines exactly when the B_0 and δB field are equal in energy, and the transition between $\langle (\delta \boldsymbol{B} \cdot \boldsymbol{B}_0)^2 \rangle_{\mathcal{V}}^{1/2} \propto \langle \delta v^2 \rangle_{\mathcal{V}}$ and $\langle \delta B^2 \rangle_{\mathcal{V}} \propto \langle \delta v^2 \rangle_{\mathcal{V}}$, as annotated in the plot.

We are able to derive the relation between $\mathcal{M}_{\rm A,turb}$ and $\mathcal{M}_{\rm A0}$ in the sub-Alfvénic regime by rearranging the coupling magnetic components, $\langle (\delta \boldsymbol{B} \cdot \boldsymbol{B}_0)^2 \rangle_{\mathcal{V}}^{1/2} = \langle \delta B_\parallel^2 \rangle_{\mathcal{V}}^{1/2} B_0$, on the right-hand side (RHS) and turbulent components on the left-hand side (LHS) of equation (19),

$$\frac{2 \langle \delta B_\parallel^2 \rangle_{\mathcal{V}}^{1/2}}{\delta v \sqrt{4\pi\rho_0}} = \mathcal{M}_{\rm A0}. \tag{30}$$

But now we need to use total fluctuating magnetic field, not just the parallel field, to get the complete $\mathcal{M}_{\rm A,turb}$. In Appendix B, we directly measure the different field components and relate them to the total fields. The most strongly anisotropic regime, in the highly sub-Alfvénic turbulence, corresponds to $(1/3) \langle \delta B_\parallel^2 \rangle_{\mathcal{V}}^{1/2} \leq \langle \delta B_\perp^2 \rangle_{\mathcal{V}}^{1/2} \leq (2/3) \langle \delta B_\parallel^2 \rangle_{\mathcal{V}}^{1/2}$ and $\langle \delta v_\parallel^2 \rangle_{\mathcal{V}}^{1/2} \approx (2/3) \langle \delta v_\perp^2 \rangle_{\mathcal{V}}^{1/2}$. For the magnetic fluctuations, we pick the average between these two values, $\langle \delta B_\perp^2 \rangle_{\mathcal{V}}^{1/2} = (1/2) \langle \delta B_\parallel^2 \rangle_{\mathcal{V}}^{1/2}$, and then propagate both the magnetic anisotropy through the regular vector magnitude equations, which gives $\langle \delta B^2 \rangle_{\mathcal{V}}^{1/2} = \sqrt{3/2} \langle \delta B_\parallel^2 \rangle_{\mathcal{V}}^{1/2}$. Substituting this back into

[9] S+2021 showed that omitting the coupling term in the estimation of the magnetic field strength in sub-Alfvénic turbulence, or equally applying the Davis (1951) and Chandrasekhar & Fermi (1953) method, can produce estimates that can be up to an order of magnitude larger than the actual values.

[10] We note there are, of course, even more definitions that one could in principle construct, for example, $\mathcal{M}_{\rm A} = \langle \delta v \rangle \sqrt{4\pi\rho_0} / \langle B \rangle$, which we use to set the Alfvén Mach number in Section 2, or one could even use component-wise constructions.

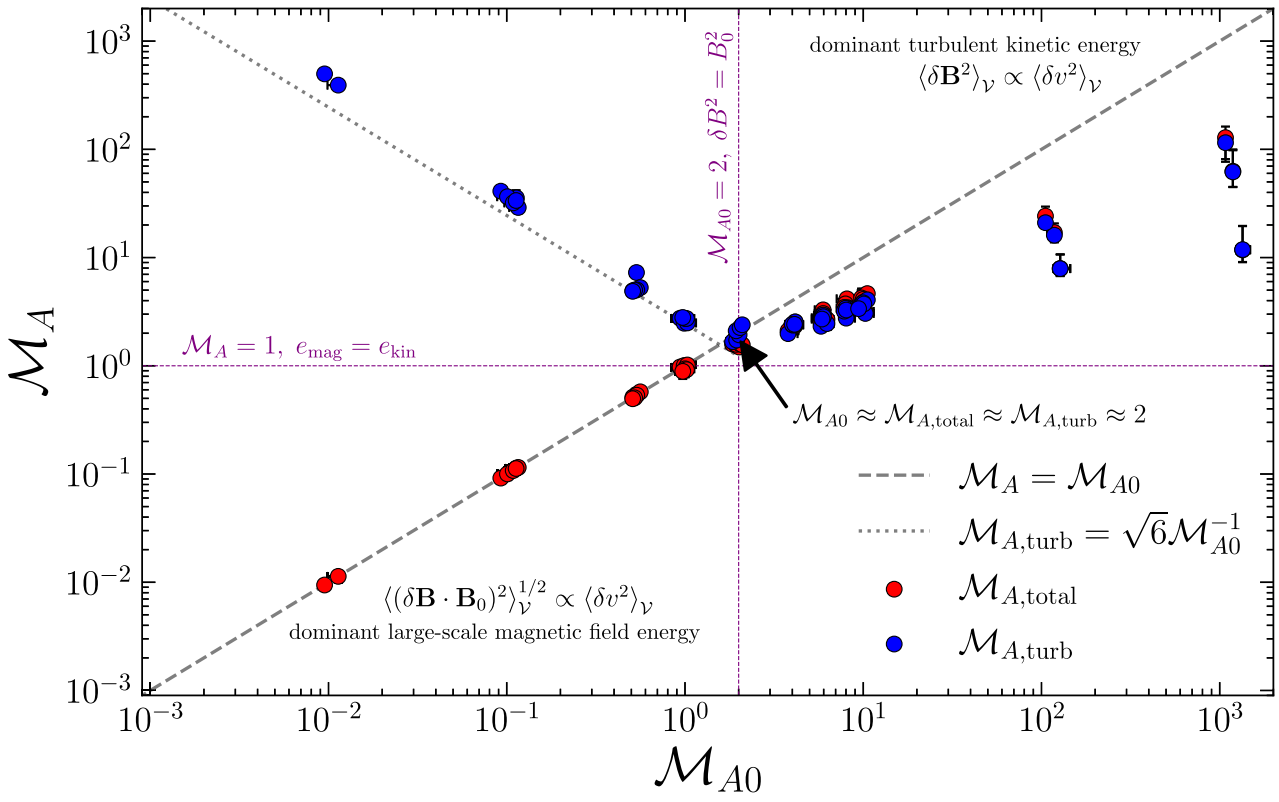

Figure 7. The total Alfvén Mach number, $\mathcal{M}_{\rm A,total}$ (equation 29), shown in red, and the turbulent Alfvén Mach number, $\mathcal{M}_{\rm A,turb}$ (equation 28), shown in blue, as a function of large-scale field Alfvén Mach number, $\mathcal{M}_{\rm A0}$ (equation 27), for all simulations. The grey dashed line is the one-to-one line between the two Alfvénic Mach numbers and $\mathcal{M}_{\rm A0}$. The dotted line shows the model for $\mathcal{M}_{\rm A,turb}$ for the $\mathcal{M}_{\rm A0} \leq 2$ (shown with vertical purple line) regime. The separation of $\mathcal{M}_{\rm A}$ into field components shows explicitly that the turbulent component of the field is highly super-Alfvénic in the sub-Alfvénic large-scale field regime (i.e. the turbulent kinetic energy is much larger than the turbulent magnetic energy, shown with the horizontal purple line), and the large-scale field dominates the total magnetic energy, $\mathcal{M}_{\rm A0} \approx \mathcal{M}_{\rm A,total}$, which coincides to $\langle (\delta \boldsymbol{B} \cdot \boldsymbol{B}_0)^2 \rangle_{\mathcal{V}}^{1/2} \propto \langle \delta v^2 \rangle_{\mathcal{V}}$, as discussed in Section 4.1. The transition into the super-Alfvénic large-scale field regime happens at a critical point in the $\mathcal{M}_{\rm A}$–$\mathcal{M}_{\rm A0}$ diagram, $\mathcal{M}_{\rm A0} \approx \mathcal{M}_{\rm A,total} \approx \mathcal{M}_{\rm A,turb} \approx 2$, where there is energy equipartition between the turbulent and large-scale magnetic field. For $\mathcal{M}_{\rm A0} > 2$, the turbulent magnetic energy is greater than the energy in the large-scale field (vertical purple line), hence $\mathcal{M}_{\rm A,turb} \approx \mathcal{M}_{\rm A,total}$, and the turbulent kinetic energy is greater than the magnetic energy, corresponding to the $\langle \delta \boldsymbol{B}^2 \rangle_{\mathcal{V}} \propto \langle \delta v^2 \rangle_{\mathcal{V}}$ regime, as discussed in Section 4.2.

equation (30) gives

$$\mathcal{M}_{\rm A,turb} = \sqrt{6}\mathcal{M}_{\rm A0}^{-1},\ \ \mathcal{M}_{\rm A0} \leq 2, \tag{31}$$

which we plot with the grey dotted line in Fig. 7. This simple model intersects with the $\mathcal{M}_{\rm A} = \mathcal{M}_{\rm A0}$ line at the $\mathcal{M}_{\rm A,total} \approx \mathcal{M}_{\rm A,turb}$ transition. At lower $\mathcal{M}_{\rm A0}$ there is some deviation away from the model, which is because of the stronger than average magnetic fluctuation anisotropy present in the $\mathcal{M}_{\rm A0} \ll 1$ data.

5.2 Hypothesis on limiting behaviour

The discussion in the preceding sections leads us to propose a hypothesis regarding the limiting behaviour of MHD turbulent systems in Fig. 7, which we illustrate schematically in Fig. 8.

5.2.1 $\mathcal{M}_{A0} \to 0$

As $\mathcal{M}_{\rm A0} \to 0$, the turbulent field should continue to become weaker and weaker ($\mathcal{M}_{\rm A,turb} \gg 1$). The reason for this is that the magnetic fluctuations (specifically the shear Alfvén waves) are smoothed out by the increasing magnetic tension, $(\boldsymbol{B} \cdot \nabla)\boldsymbol{B}$, and are reduced in

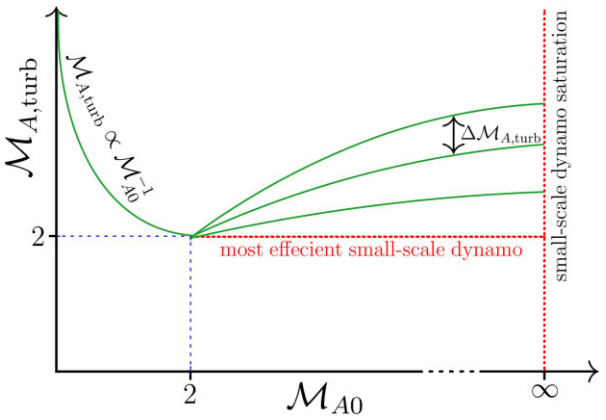

Figure 8. Schematic for the $\mathcal{M}_{\rm A,turb}$–$\mathcal{M}_{\rm A0}$ plane, showing the small-scale dynamo saturation in the $\mathcal{M}_{\rm A0} \to \infty$ limit, and the $\mathcal{M}_{\rm A,turb} \propto \mathcal{M}_{\rm A0}^{-1}$ $\left(\langle \delta B^2 \rangle_{\mathcal{V}_L}^{1/2} \propto B_0^{-1}\right)$ power law in the $\mathcal{M}_{\rm A0} \to 0$ limit, derived using energy balance. The separation between $\mathcal{M}_{\rm A,turb}(\mathcal{M}_{\rm A0})$ curves, $\Delta\mathcal{M}_{\rm A,turb}$, changes with different plasma parameters that control the small-scale dynamo saturation.

degrees of freedom since they are perfectly flux frozen into $\boldsymbol{B}_0$. Therefore, instead of any field-line stretching, coherent magnetic field lines are randomly walked in the perpendicular plane to $\boldsymbol{B}_0$ (field line random walk; Jokipii & Parker 1968). 2D planar motions cannot instigate dynamo action (Zel'dovich 1957 theorem), so it is unlikely that δB ever grows irreversibly[11] again in this limit, and we find $\langle \delta B^2 \rangle_{\mathcal{V}_L}^{1/2} \propto B_0^{-1}$ (equation 31; consistent with qualitative observations in previous studies; Haugen, Brandenburg & Dobler 2004), until the magnetic field only has a large-scale component and $B = B_0$.

5.2.2 $\mathcal{M}_{A0} \rightarrow \infty$

In the $\mathcal{M}_{\rm A0} \rightarrow \infty$ ($B_0 \rightarrow 0$) limit, we reach the results from the small-scale dynamo community. Very broadly speaking, in these studies, where $B_0 = 0$, and hence $\mathcal{M}_{\rm A0} \rightarrow \infty$, the equilibrium magnetic field strength asymptotes to a value that depends on the sonic Mach number and ratio of compressive to solenoidal modes in the turbulence, and plasma Reynolds numbers (if they are finite). In this limit, the maximally efficient turbulent dynamo is for the most subsonic, solenoidal flows and the least efficient for the highest $\mathcal{M}$, most compressible flows (Federrath et al. 2014; Schober et al. 2015; Federrath 2016; Achikanath Chirakkara et al. 2021). Hence, as $\mathcal{M}_{\rm A0}$ becomes larger, we should expect to observe the $\mathcal{M}_{\rm A}(\mathcal{M}_{\rm A0})$ curves separate and asymptote to different constant values of $\mathcal{M}_{\rm A,turb}$ as a function of $\mathcal{M}$, which is what we find in Fig. 7. Since the most efficient turbulent dynamo[12] leads to saturation of $\mathcal{M}_{\rm A,total} \approx 2$ (see highly subsonic, solenoidal experiments in Achikanath Chirakkara et al. 2021), this defines a floor that bounds $\mathcal{M}_{\rm A}$ from below as $\mathcal{M}_{\rm A0} \rightarrow \infty$.

5.3 Sub-Alfvénic turbulent fields do not exist

We find that the fluctuating magnetic field becomes extremely weak at $\mathcal{M}_{\rm A0} < 2$, and is bounded from below by the most efficient saturation of the small-scale dynamo in the limit $\mathcal{M}_{\rm A0} \rightarrow \infty$. An immediate consequence of these two limiting behaviours is that there is no room in the $\mathcal{M}_{\rm A}$–$\mathcal{M}_{\rm A0}$ plane for $\mathcal{M}_{\rm A,turb} \lesssim 2$ turbulence. Hence the only sub-Alfvénic turbulence that is possible in this parameter space is sub-Alfvénic *large-scale field* (or coherent field) fluid turbulence. We show that this kind of turbulence is highly super-Alfvénic with respect to the turbulent velocity fluctuations (shocks and vortices), $\mathcal{M}_{\rm A,turb} \gg 1$, and it is only through the non-turbulent components of the plasma that the magnetic energy is able to be sufficiently stronger than the kinetic energy. As a caveat of this analysis, in this section, we volume-averaged the plasma beyond the correlation scale of the turbulence, hence this does not rule out that the turbulence can be sub-Alfvénic on scales much smaller than the correlation scale. In the next section, we explore averaging below the correlation scale, and discuss how sub-Alfvénic turbulence can emerge by taking statistics below the correlation scale.

[11]Note that it may grow locally, through reversible processes such as compression, but these ought to average out over time.

[12]Note this is in absence of magnetic helicity, which may significantly change the saturation of the dynamo given that there are more degrees of freedom to store magnetic energy than in non-helical turbulence and magnetic modes above the outer scale of the turbulence can be energized (e.g. sections 4–5 in Rincon 2019).

6 THE AVERAGING SCALE

We have shown it is important to average equation (9) in such a way that all of the terms are positive definite, and that $\langle (\delta \boldsymbol{B} \cdot \boldsymbol{B}_0)^2 \rangle_{\mathcal{V}}^{1/2}$ balances the kinetic turbulent energy perfectly in the sub-Alfvénic large-scale field turbulence regime. However, these methods critically rely on an averaging scale $\mathcal{V}$. In this section, we highlight the importance of $\mathcal{V}$ and show that even if one adopts the traditional ansatz that does not enforce positivity, equation (10), the coupling term can make non-zero contributions to the turbulent energy.

The fundamental reason for this is that the volume-averaging scale for $\langle \cdots \rangle_{\mathcal{V}}$ is important. In simulations, we regularly report volume-averaged statistics over a few turbulent correlation scales, $\ell_{{\rm cor},v}$, i.e. $\mathcal{V} = \bigcup_{i=1}^{N} (\ell_{{\rm cor},v}^3)_i$, where N is a few, or directly at the full size of a simulation box, $\mathcal{V} = \mathcal{V}_L$. However, for many observations of the ISM, the region sampled is far smaller than the turbulent correlation scale. For example, magnetic fields in star-forming clouds are observed to be correlated on scales up to ~100 pc (Li et al. 2014), comparable to the scale height and the outer scale of turbulence in galactic discs (e.g. Karlsson, Bromm & Bland-Hawthorn 2013; Falceta-Gonçalves et al. 2014; Krumholz & Ting 2018). Dust polarization observations using *Herschel* (e.g. the *Herschel* Gould Belt Survey; André et al. 2010) generally sample[13] much smaller fields of view (of order 10 pc); over size scales typically probed by such observations, there is no sign of a flattening in the velocity dispersion–size relation (Federrath et al. 2021; Yun et al. 2021; Zhou, Li & Chen 2022), clear evidence that the region being studied is much smaller than the correlation scale.

To explore the implications of this, we directly compute the correlation scales of the turbulence $\ell_{{\rm cor},v}$ and magnetic field $\ell_{{\rm cor},B}$ in our simulations, and plot them as a function of $\mathcal{M}_{\rm A0}$, coloured by $\mathcal{M}$ in Fig. 9. We compute both of them in the textbook manner, directly from the energy spectra $\mathscr{P}_v(k)$ and $\mathscr{P}_B(k)$ as

$$\frac{\ell_{\rm cor}}{\ell_0} = \frac{L}{\ell_0} \frac{\int_0^\infty {\rm d}k\, k^{-1} \mathscr{P}(k)}{\int_0^\infty {\rm d}k\, \mathscr{P}(k)}, \tag{32}$$

where $\mathscr{P}(k)$ is replaced by $\mathscr{P}_v(k)$ for the turbulence correlation scales, and $\mathscr{P}_B(k)$ for the magnetic field correlation scales.

We focus first on the top panel of Fig. 9, the turbulence correlation scale. The super-Alfvénic large-scale field experiments have $\ell_{{\rm cor},v} \approx \ell_0$, with a small dip at $\mathcal{M}_{\rm A0} = 2$ as the turbulence transitions between $\boldsymbol{B}_0$ and $\delta \boldsymbol{B}$ dominated (as discussed in Section 3). The sub-Alfvénic turbulence has correlations scales above the driving scale, most likely due to the system-scale vortices that develop in the flow (Beattie et al. 2020, 2021b). If we interpret this experiment at face value, this means that if individual clouds are sub-Alfvénic, we should expect correlated turbulent velocities beyond the extent of the entire sub-Alfvénic region, even if the driving scale is not itself larger than the individual clouds. For the ISM in general, which is probably trans-Alfvénic-to-super-Alfvénic ($\mathcal{M}_{\rm A0} \approx 2$) and transonic on average (Gaensler et al. 2011; Krumholz et al. 2020; Seta & Federrath 2021b; Liu et al. 2022), we should expect turbulent motions to be correlated out to the driving scale of the largest turbulent motions. This, of course, is a natural repercussion of one of the central tenets of turbulence: the energy cascade from large (galactic, in this context) to small (molecular cloud and smaller; Armstrong, Rickett & Spangler 1995) scales.

[13]In observations we can define a sampling scale as the maximum spatial separation of observational data in the plane of the sky.

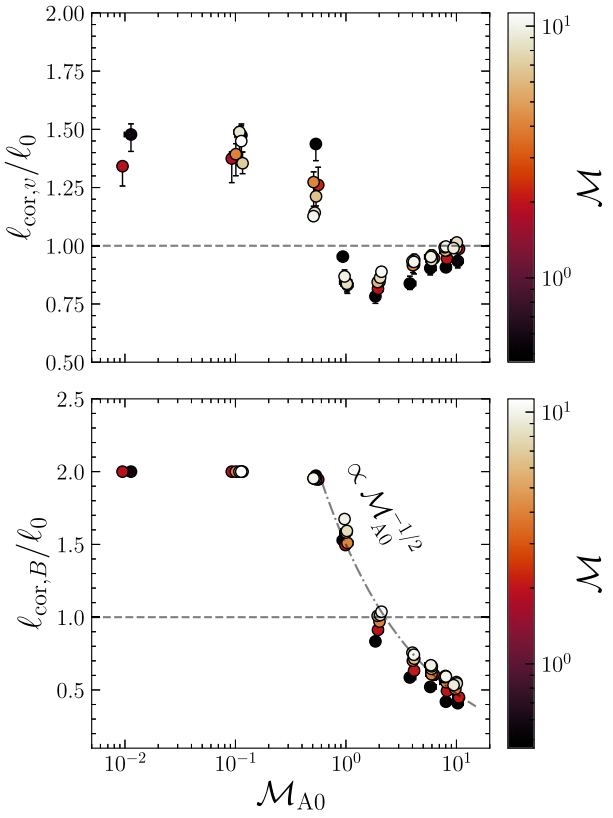

Figure 9. Top: the turbulent correlation scale, $\ell_{\rm cor,\,v}$ (equation 32), in units of turbulent driving scale, ℓ_0, as a function of $\mathcal{M}_{\rm A0}$, for all simulations. We find $\ell_{\rm cor,\,v} \approx \ell_0$, with some systematic deviation at low $\mathcal{M}_{\rm A0}$, most likely due to the strong, global anisotropy in those simulations. Bottom: the same, but for the correlation scale of the magnetic field, $\ell_{\rm cor,\,B}$. The scatter at each $\mathcal{M}_{\rm A0}$ is determined by $\mathcal{M}$, which ranges between $\mathcal{M} \approx 0.5$ and 10 and only weakly changes the correlation scale of the turbulence.

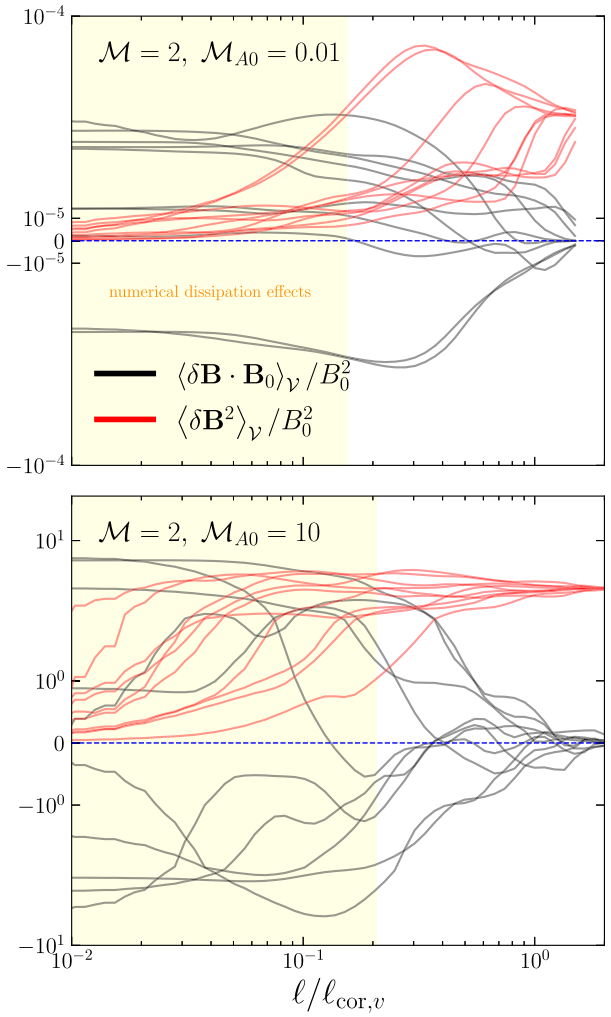

Figure 10. Coupling and mean-squared values of magnetic fluctuation terms in units of large-scale field as a function of averaging scale normalized to the correlation scale of the turbulence, $\ell_{\rm cor,\,v}$, for the 10 randomly sampled regions in the `M2MA001` (top) and `M2MA10` (bottom) simulations. The square magnitude of $\delta\boldsymbol{B}$ on scale $\ell/\ell_{\rm cor,\,v}$ is shown in red, and the mean of $\delta\boldsymbol{B}\cdot\boldsymbol{B}_0$ on that scale is shown in black. The yellow shaded region indicates where numerical dissipation effects may influence the field statistics. Because of the spatial correlation of the magnetic field, on scales $\ell < \ell_{\rm cor,\,v}$ (volumes $\mathcal{V} \lesssim \ell^3_{\rm cor,\,v}$), turbulent fields are converted into effective mean fields. This means $\langle \delta\boldsymbol{B}\cdot\boldsymbol{B}_0\rangle_{\mathcal{V}} \neq 0$ on scales below $\ell_{\rm cor,\,v}$, acting as an effective mean field on that scale. On scales above $\ell_{\rm cor,\,v}$ the Reynolds rule of averaging holds and $\langle \delta\boldsymbol{B}\cdot\boldsymbol{B}_0\rangle_{\mathcal{V}} = 0$ as expected.

Similar to the turbulence correlation scales, the magnetic correlation scales of the sub-Alfvénic simulations are on larger scales than the driving scale, indicating, as we showed in Section 5, that the fluctuating magnetic field is negligible in the sub-Alfvénic regime, and is strongly suppressed by the large-scale field. The super-Alfvénic simulations show a decaying power law $\ell_{\rm cor,\,B} \propto \ell_0 \mathcal{M}_{\rm A0}^{-1/2}$, which demonstrates that as the large-scale field weakens, the causally connected regions in the magnetic field move to smaller and smaller scales (qualitatively consistent with previous expectations; e.g. Lazarian & Beresnyak 2006). This is likely due to the strong turbulent motions tangling the magnetic field (e.g. section 4.1.1 in Sampson et al. 2022), increasing the net curvature (Yuen & Lazarian 2020) and facilitating a smaller scale field.[14] This means, to place the correlation scale of the magnetic field on comparable scales of a 10 pc observation (e.g. Federrath et al. 2016; Panopoulou, Psaradaki & Tassis 2016; Beattie et al. 2019; Hu et al. 2019), for $\ell_0 = 100$ pc we require that $\mathcal{M}_{\rm A0} \gtrsim 100$, which on average is unrealistically high for the $\mathcal{M}_{\rm A0}$ in the disc of Milky Way analogues (Hopkins et al. 2021; Wibking & Krumholz 2021). Likewise, for average ISM parameters that we use from the above discussion ($\ell_0 = 100$ pc, $\mathcal{M}_{\rm A0} = 2$), $\ell_{\rm cor,\,B} \propto \ell_0 \mathcal{M}_{\rm A0}^{-1/2}$ gives $\ell_{\rm cor,\,B} \approx 70$ pc, which determines the largest scale in which the magnetic field can be casually connected via magnetic field fluctuations, when driven at 100 pc.

The significance of this for magnetic energy balance, in both simulations and observations, is that we are often dealing with volumes $\mathcal{V} \ll \mathcal{V}_L$, and while $\langle \delta\boldsymbol{B}\cdot\boldsymbol{B}_0\rangle_{\mathcal{V}_L} = 0$, in general $\langle \delta\boldsymbol{B}\cdot\boldsymbol{B}_0\rangle_{\mathcal{V}} \neq 0$ when $\mathcal{V} < \mathcal{V}_L$. More generally, for random fields $\boldsymbol{X}$ and $\boldsymbol{Y}$, averaged on volumes $\mathcal{V} < \mathcal{V}_L$, $\langle\langle \boldsymbol{X}\rangle_{\mathcal{V}}\,\boldsymbol{Y}\rangle_{\mathcal{V}} \neq \langle \boldsymbol{X}\rangle_{\mathcal{V}}\,\langle \boldsymbol{Y}\rangle_{\mathcal{V}}$ and without loss of generality, $\langle \delta\boldsymbol{X}\rangle_{\mathcal{V}} \neq 0$, i.e. the Reynolds rule of averaging is no longer valid (Germano 1992; Hollins et al. 2018). We show an explicit example of this for sub-Alfvénic `M2MA001` (top) and super-Alfvénic `M2MA10` (bottom) simulations, mimicking the transonic average ISM in Fig. 10. We provide a full description of the methodology for performing the experiment in Appendix C, but to summarize here, we use real-space spherical top-hat filters initialized at random

[14] In the sense that the ratio of the magnetic energy in the low-k modes to the magnetic energy in the high-k modes is shrinking.

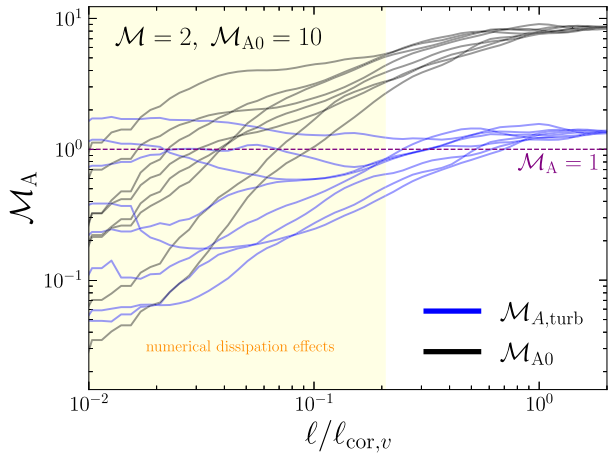

Figure 11. The same as the bottom panel of Fig. 10, but for the scale-dependent Alfvén Mach numbers of the large-scale field, equation (27), and the turbulent field, equation (28).

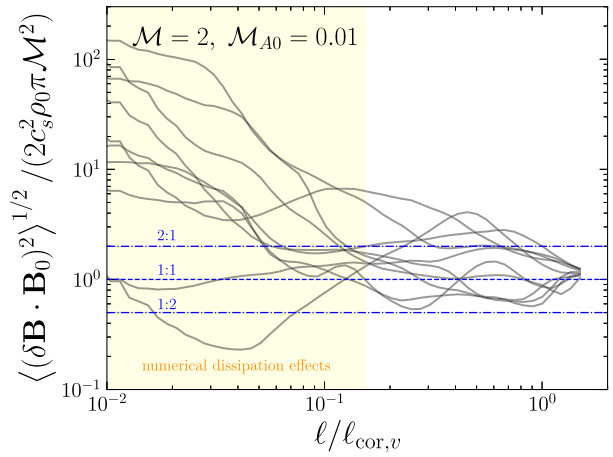

Figure 12. The same as the top panel of Fig. 10, but for the scale-dependent energy balance, in the strong-field limit equation (19). We show lines of 1:1 (blue, dashed), 2:1 and 1:2 (blue, dot–dashed), highlighting that between the largest scales in the simulations and the dissipation scales (indicated with the yellow shaded region) almost all of the random regions sampled fall within a factor of 2 in exact equipartition.

coordinates in each the simulation, each with diameters $\ell/\ell_{{\rm cor},v}$, to compute the mean-squared (red) and mean (black) of the filtered $\delta\boldsymbol{B}$ and $\delta\boldsymbol{B}\cdot\boldsymbol{B}_0$ fields, in units of the large-scale field, respectively; $\ell_{{\rm cor},v}$ is computed independently, directly from the velocity power spectra, equation (32). We indicate in yellow the scales for which numerical dissipation may influence the rms statistics, which can be up to ∼30 grid cells for our (and other grid) simulation solvers (see section 2 in Kitsionas et al. 2009; Federrath et al. 2011b, for further details).

For both simulations, we find that on scales $\ell < \ell_{{\rm cor},v}$, $\left\langle \delta\boldsymbol{B}\cdot\boldsymbol{B}_0(\ell/\ell_{{\rm cor},v})\right\rangle_{\mathcal{V}} \neq 0$, coupled with a small $\left\langle \delta\boldsymbol{B}^2(\ell/\ell_{{\rm cor},v})\right\rangle_{\mathcal{V}}$ compared to the system-scale $\left\langle \delta\boldsymbol{B}^2\right\rangle_{\mathcal{V}}$. This is a natural repercussion of finite spatial correlation in the plasma, where local regions in the turbulence, $\ell^3 < \ell^3_{{\rm cor},v}$, can have fields that appear ordered, even though they are part of the global fluctuating field, as evident from Fig. 10. When averaging over these filtered regions the spatially correlated fluctuating field acts as an effective large-scale field on that scale. The main difference between the two simulations is the size of the fluctuating field, which is orders of magnitude smaller on all scales in the sub-Alfvénic simulation, as expected from our previous discussions in Section 5. Our analysis also illustrates the difficulty of distinguishing between large- and small-scale magnetic fields when one is making observations well below $\ell_{{\rm cor},v}$, and provides a very clear reason why $\delta\boldsymbol{B}\cdot\boldsymbol{B}_0$ may be an important quantity for magnetic field observations made over a finite field of view. This finding has strong implications for the interpretation of observations. As we discussed in Section 1, some ISM observations suggest that clouds are in a sub-Alfvénic state (Li et al. 2013; Federrath et al. 2016; Hu et al. 2019; Heyer et al. 2020; Hwang et al. 2021; Skalidis et al. 2021b; Hoang et al. 2022). Based on our analysis in Section 5, this means that a very strong, large-scale field must be present. Naively, the small-scale dynamo, which is generally invoked to explain the magnetic field strengths in the ISM, should not be able to maintain such a system (the most efficient dynamo saturates at $\mathcal{M}_{\rm A} \approx 2$; Federrath 2016), with all of the magnetic energy being stored in the large-scale field. An α–Ω dynamo that can grow a large-scale, coherent magnetic field through the Parker loops (α; Parker 1979) or differential, possibly galactic, rotation (Ω; see section 2.6 in Beck & Wielebinski 2013) may be required to grow such a field at the kpc scale, which is coupled to the ISM of the galaxy, piercing individual clouds and making them highly magnetized.

Our current analysis suggests an alternative possibility: one way of creating an effective mean field, which may act like a large-scale field for scales below it (e.g. for a sub-Alfvénic plasma embedded in a super-Alfvénic plasma), is by taking filtered statistics of the turbulence, and hence observing the fluctuating field well below the correlation scale of the turbulence. Because this process turns fluctuating field into an effective large-scale field, it facilitates the perfect conditions for moving left in Fig. 7, with subdominant magnetic field fluctuations and a strong coherent field. In Fig. 11, we show the same filtered turbulence calculation as in Fig. 10 but now instead with $\mathcal{M}_{\rm A0}(\ell/\ell_{{\rm cor},v})$ (black curve) and $\mathcal{M}_{\rm A,turb}(\ell/\ell_{{\rm cor},v})$ (blue curve). We use the `M2MA10` simulation, which is globally super-Alfvénic, $\mathcal{M}_{\rm A0}(L/\ell_{{\rm cor},v}) \approx 10$, as indicated to the far right of the black curve. On scales smaller than the $\ell_{{\rm cor},v}$, a majority of the random samples exhibit $\mathcal{M}_{\rm A,turb}(\ell/\ell_{{\rm cor},v}) < 1$, and likewise for $\mathcal{M}_{\rm A0}(\ell/\ell_{{\rm cor},v})$, albeit over a narrower range in $\ell/\ell_{{\rm cor},v}$. In the context of simulations, this shows that the statistics of small regions in the turbulence can be effectively sub-Alfvénic, even in a globally super-Alfvénic plasma. In the context of observations of the cold, molecular ISM, it means that even though individual clouds may be observed to be sub-Alfvénic, the magnetic fields in these clouds may still be the result of a small-scale dynamo process, saturating at super-Alfvénic values, but operating on scales much larger than the cloud being observed. Thus observing a cloud to be sub-Alfvénic, $\mathcal{M}_{\rm A} \lesssim 2$, does *not* automatically mean that the field in that cloud is the product of an α–Ω or similar large-scale dynamo; one can conclude that such a process is at work only if one recovers $\mathcal{M}_{\rm A} \lesssim 2$ *on scales larger than the turbulent correlation length*.

As a final calculation for this study, we compute the energy ratio of the coupling term to the kinetic energy, $\left\langle (\delta\boldsymbol{B}\cdot\boldsymbol{B}_0)^2\right\rangle_{\mathcal{V}}^{1/2}/(2c_{\rm s}^2\rho_0\pi\mathcal{M}^2)$ (the ratio of the left- to right-hand side of equation 19) in a sub-Alfvénic plasma as a function of scale, just as we did in the previous paragraphs for the other rms statistics. This tests if the energy balance we presented in Section 3 is valid over a range of scales, necessary for making it a useful relation for applications. We plot $\left\langle (\delta\boldsymbol{B}\cdot\boldsymbol{B}_0)^2\right\rangle_{\mathcal{V}}^{1/2}/(2c_{\rm s}^2\rho_0\pi\mathcal{M}^2)$ as a function of $\ell/\ell_{{\rm cor},v}$ in Fig. 12, for the same simulation as in the top panel of Fig. 10. We find that on the

interval between the system scale L and the scale in which numerical dissipation effects exist ℓ_ν (the largest scale that is shaded yellow) that our filtered samples of the turbulence mostly fall within the 1:2 to 2:1 interval (blue, dot–dashed lines). On average, across all samples and $\ell \in [\ell_\nu, L]$, we find $\left\langle (\delta \boldsymbol{B} \cdot \boldsymbol{B}_0)^2 \right\rangle_{\mathcal{V}}^{1/2} / (2 c_s^2 \rho_0 \pi \mathcal{M}^2) = 1.5 \pm 1$, capturing the exact equipartition within 0.5σ. Below ℓ_ν most of the samples become highly magnetized due to the kinetic energy being dominated by numerical dissipation and the large-scale magnetic field permeating through all of the scales in the plasma.

7 SUMMARY AND KEY FINDINGS

Motivated by recent works on measuring and modelling magnetic fields in the ISM (Beattie & Federrath 2020; Skalidis & Tassis 2021; S+2021), we provide a theoretical and numerical exposition of the rms energy balance between the kinetic and magnetic energy, highlighting the role of the magnetic coupling term, $\left\langle (\delta \boldsymbol{B} \cdot \boldsymbol{B}_0)^2 \right\rangle_{\mathcal{V}}^{1/2}$, which describes the energy contained in magnetic fluctuations $\delta \boldsymbol{B}$ coupled to the large-scale magnetic field $\boldsymbol{B}_0$. We discuss the significance of this term in the context of the first (comparing volume-averaged energies) and second (comparing magnitudes of energy fluctuations) moments of the energy balance equations, deriving its typical value directly from the second moment equations, which preserve the positivity of each energy contribution. From this argument we derive a number of analytical models with no free parameters, for the coupling term and fluctuating magnetic field, $\delta \boldsymbol{B}$, and demonstrate that these yield outstanding agreement with the results of a large suite of MHD simulations. Our analysis demonstrates that $\left\langle (\delta \boldsymbol{B} \cdot \boldsymbol{B}_0)^2 \right\rangle_{\mathcal{V}}^{1/2}$ plays an important role in sub-to-trans-Alfvénic large-scale field turbulence, regardless of the sonic Mach number $\mathcal{M}$. This term becomes less important for $\mathcal{M}_{\rm A0} > 2$, where δB^2 becomes dominant, but the large-scale field still has an effect. In Section 5, we explore three different formulations of the Alfvénic Mach number $\mathcal{M}_{\rm A}$, and the relations between them, showing that sub-Alfvénic *large-scale* field turbulence, supports an extremely super-Alfvénic turbulent field, suggesting that the magnetic field fluctuations are smaller than velocity fluctuations in this limit. We present a heuristic for understanding the whole turbulent and large-scale field Alfvén Mach number parameter plane and discuss the implications for interpreting ISM observations and sub-Alfvénic turbulence. We list the key results of this study below.

(i) We provide theoretical models for the volume-averaged fluctuating and coupling magnetic fields, $\left\langle \delta \boldsymbol{B}^2 \right\rangle$ and $\left\langle (\delta \boldsymbol{B} \cdot \boldsymbol{B}_0)^2 \right\rangle_{\mathcal{V}}^{1/2}$, assuming energy equipartition between $\left\langle (\delta \boldsymbol{B} \cdot \boldsymbol{B}_0)^2 \right\rangle_{\mathcal{V}}^{1/2}$ and the volume-averaged velocity fluctuations $\left\langle \delta v^2 \right\rangle_{\mathcal{V}}$ in the sub-Alfvénic regime (equations 20 and 22), and $\left\langle \delta \boldsymbol{B}^2 \right\rangle_{\mathcal{V}}$ and $\left\langle \delta v^2 \right\rangle_{\mathcal{V}}$ in the super-Alfvénic regime (equations 24 and 25). These models are free of parameters, but rely on the numerical observation that $\langle \delta v^2 \rangle \approx \langle \delta v^4 \rangle^{1/2}$ and $\langle \delta B^2 \rangle \approx \langle \delta B^4 \rangle^{1/2}$, i.e. that the average energy scales with the magnitude of energy fluctuations, which we demonstrate in Fig. 3. Our models show excellent agreement with numerical compressible MHD data, over a very broad range of plasma values, in Figs 4–6. We discuss how this provides strong support for the polarization dispersion models [Davis–Chandrasekhar–Fermi (DCF)-like methods] derived in Skalidis & Tassis (2021) and S+2021.

(ii) We define large-scale field, turbulent, and total Alfvén Mach numbers (Section 5) and propose that we can completely define the whole $\mathcal{M}_{\rm A,turb}$–$\mathcal{M}_{\rm A0}$ data plane, shown in Fig. 8, based on the small-scale dynamo saturation as $\mathcal{M}_{\rm A0} \to \infty$, and an analytical model that we derive using energy balance for $\mathcal{M}_{\rm A0} \to 0$, equation (31), which implies $\left\langle \delta B^2 \right\rangle_{\mathcal{V}_L}^{1/2} \propto B_0^{-1}$. Critically, we show that the turbulent magnetic field never becomes sub-Alfvénic, and it is only through a strong, large-scale magnetic field that the turbulence can transition into this regime. We show that the turbulence becomes highly super-Alfvénic in the sub-Alfvénic large-scale field regime, and discuss the implications for sub-Aflvénic ISM observations in Section 5.3. We suggest that a contributing factor to sub-Alfvénic ISM observations may be from measuring a trans-to-super Alfvénic average ISM, which, unlike sub-Alfvénic turbulence, may be supported by a small-scale dynamo, well below the correlation scale of the turbulence. We show that this is true for simulations of globally super-Alfvénic turbulence in Fig. 11.

(iii) In Fig. 10, we explicitly show that by measuring filtered magnetic field statistics below the correlation scale of the turbulence (equation 32), which is roughly equal to the driving scale with some slight deviations in the sub-Alfvénic regime (Fig. 9), one turns the fluctuating field into an effective mean field. We show this is true for both the sub-Alfvénic and super-Alfvénic regime. This highlights that for quantities such as $\langle \delta \boldsymbol{B} \cdot \boldsymbol{B}_0 \rangle_{\mathcal{V}}$ or $\left\langle \delta \boldsymbol{B}^2 \right\rangle_{\mathcal{V}}$, if the volume-averaging scale, $\mathcal{V}$, does not resolve the correlation scale of the turbulence, then the volume average need not be zero, as previously discussed in Germano (1992) and Hollins et al. (2018). Furthermore, in Fig. 12, we show our sub-Alfvénic energy balance model provides good agreement across the resolved scales available to us in the sub-Alfvénic regime.

ACKNOWLEDGEMENTS

We thank the anonymous referee for the useful suggestions that increased the quality of our study. JRB thanks Christoph Federrath's and Mark Krumholz's research groups for many productive discussions and acknowledges financial support from the Australian National University, via the Deakin PhD and Dean's Higher Degree Research (theoretical physics) Scholarships and the Australian Government via the Australian Government Research Training Program Fee-Offset Scholarship. MRK acknowledges support from the Australian Research Council's *Discovery Projects* scheme, award DP190101258. RS acknowledges financial support from the European Research Council (ERC) under the European Union's Horizon 2020 Framework Programme under grant agreement no. 771282. CF acknowledges funding provided by the Australian Research Council (Future Fellowship FT180100495), and the Australia–Germany Joint Research Cooperation Scheme (UA-DAAD). JRB and CF further acknowledge high-performance computing resources provided by the Leibniz-Rechenzentrum and the Gauss Centre for Supercomputing (grants pr32lo, pn73fi, and GCS Large-scale project 22542), and the Australian National Computational Infrastructure (grant ek9) in the framework of the National Computational Merit Allocation Scheme and the ANU Merit Allocation Scheme.

The simulation software, FLASH, was in part developed by the Flash Centre for Computational Science at the Department of Physics and Astronomy of the University of Rochester. Data analysis and visualization software used in this study: c++ (Stroustrup 2013), NUMPY (Oliphant 2006; Harris et al. 2020), MATPLOTLIB (Hunter 2007), CYTHON (Behnel et al. 2011), VISIT (Childs et al. 2012), SCIPY (Virtanen et al. 2020), and SCIKIT-IMAGE (van der Walt et al. 2014).

DATA AVAILABILITY

The data underlying this paper will be shared on reasonable request to the corresponding author.

REFERENCES

Acharya B. et al., 2022, Nature, 602, 63
Achikanath Chirakkara R., Federrath C., Trivedi P., Banerjee R., 2021, Phys. Rev. Lett., 126, 091103
Allys E., Levrier F., Zhang S., Colling C., Regaldo-Saint Blancard B., Boulanger F., Hennebelle P., Mallat S., 2019, A&A, 629, A115
André P. et al., 2010, A&A, 518, L102
Armstrong J. W., Rickett B. J., Spangler S. R., 1995, ApJ, 443, 209
Beattie J. R., Federrath C., 2020, MNRAS, 492, 668
Beattie J. R., Federrath C., Klessen R. S., Schneider N., 2019, MNRAS, 488, 2493
Beattie J. R., Federrath C., Seta A., 2020, MNRAS, 498, 1593
Beattie J. R., Mocz P., Federrath C., Klessen R. S., 2021a, MNRAS, 504, 4354
Beattie J. R., Mocz P., Federrath C., Klessen R. S., 2021b, MNRAS, preprint (arXiv:2109.10470)
Beattie J. R., Krumholz M. R., Federrath C., Sampson M., Crocker R. M., 2022, preprint (arXiv:2203.13952)
Beck R., Wielebinski R., 2013, in Oswalt T. D., Gilmore G., eds, Planets, Stars and Stellar Systems. Vol. 5: Galactic Structure and Stellar Populations. Springer, Dordrecht, p. 641
Behnel S., Bradshaw R., Citro C., Dalcin L., Seljebotn D. S., Smith K., 2011, Comput. Sci. Eng., 13, 31
Bhattacharjee A., Ng C. S., Spangler S. R., 1998, ApJ, 494, 409
Biermann L., 1950, Z. Nat. Teil A, 5, 65
Boldyrev S., 2006, Phys. Rev. Lett., 96, 115002
Bouchut F., Klingenberg C., Waagan K., 2010, Numer. Math., 115, 647
Bruno R., Carbone V., 2013, Living Rev. Sol. Phys., 10, 2
Brunt C. M., Federrath C., 2014, MNRAS, 442, 1451
Brunt C. M., Heyer M. H., Mac Low M. M., 2009, A&A, 504, 883
Brunt C. M., Federrath C., Price D. J., 2010a, MNRAS, 403, 1507
Brunt C. M., Federrath C., Price D. J., 2010b, MNRAS, 405, L56
Burkhart B., 2018, ApJ, 863, 118
Burkhart B., 2021, PASP, 133, 102001
Chandrasekhar S., Fermi E., 1953, ApJ, 118, 113
Childs H. et al., 2012, in Bethel E. W., Childs H., Hansen C., eds, High Performance Visualization: Enabling Extreme-Scale Scientific Insight. Taylor & Francis, Oxfordshire, UK, p. 357
Colling C., Hennebelle P., Geen S., Iffrig O., Bournaud F., 2018, A&A, 620, A21
Davis L., 1951, Phys. Rev., 81, 890
Dubey A. et al., 2008, in Pogorelov N. V., Audit E., Zank G. P., eds, ASP Conf. Ser. Vol. 385, Numerical Modeling of Space Plasma Flows: Astronum-2007. Astron. Soc. Pac., San Francisco, p. 145
Elmegreen B. G., 2009, in Andersen J., Bland-Hawthorn J., Nordströaram B., eds, Proc. IAU Symp. Vol. 254, The Galaxy Disk in Cosmological Context. Cambridge Univ. Press, Cambridge, p. 289
Falceta-Gonçalves D., Kowal G., Falgarone E., Chian A. C.-L., 2014, Nonlinear Processes Geophys., 21, 587
Federrath C., 2013, MNRAS, 436, 1245
Federrath C., 2015, MNRAS, 450, 4035
Federrath C., 2016, J. Plasma Phys., 82, 535820601
Federrath C., Klessen R. S., 2012, ApJ, 761, 156
Federrath C., Klessen R. S., Schmidt W., 2008, ApJ, 688, L79
Federrath C., Klessen R. S., Schmidt W., 2009, ApJ, 692, 364
Federrath C., Roman-Duval J., Klessen R. S., Schmidt W., Mac Low M.-M., 2010, A&A, 512, A81
Federrath C., Chabrier G., Schober J., Banerjee R., Klessen R. S., Schleicher D. R. G., 2011a, Phys. Rev. Lett., 107, 114504
Federrath C., Sur S., Schleicher D. R. G., Banerjee R., Klessen R. S., 2011b, ApJ, 731, 62
Federrath C., Schober J., Bovino S., Schleicher D. R. G., 2014, ApJ, 797, L19
Federrath C. et al., 2016, ApJ, 832, 143
Federrath C. et al., 2017a, in Crocker R. M., Longmore S. N., Bicknell G. V., eds, Proc. IAU Symp. Vol. 322, The Multi-Messenger Astrophysics of the Galactic Centre. Cambridge Univ. Press, Cambridge, p. 123
Federrath C., Krumholz M., Hopkins P. F., 2017b, J. Phys.: Conf. Ser., 837, 012007
Federrath C., Klessen R. S., Iapichino L., Beattie J. R., 2021, Nat. Astron., 5, 365
Federrath C., Roman-Duval J., Klessen R. S., Schmidt W., Mac Low M.-M., 2022, Astrophysics Source Code Library, record ascl:2204.001
Fryxell B. et al., 2000, ApJS, 131, 273
Gaensler B. M. et al., 2011, Nature, 478, 214
Galishnikova A. K., Kunz M. W., Schekochihin A. A., 2022, preprint (arXiv:2201.07757)
Germano M., 1992, J. Fluid Mech., 238, 325
Goldreich P., Sridhar S., 1995, ApJ, 438, 763
Grisdale K., Agertz O., Romeo A. B., Renaud F., Read J. I., 2017, MNRAS, 466, 1093
Harris C. R. et al., 2020, Nature, 585, 357
Hartlep T., Matthaeus W. H., Padhye N. S., Smith C. W., 2000, J. Geophys. Res., 105, 5135
Haugen N. E. L., Brandenburg A., Dobler W., 2004, Ap&SS, 292, 53
Hennebelle P., Chabrier G., 2009, ApJ, 702, 1428
Hennebelle P., Inutsuka S.-i., 2019, Frontiers Astron. Space Sci., 6, 5
Hennebelle P., Commerçon B., Joos M., Klessen R. S., Krumholz M., Tan J. C., Teyssier R., 2011, A&A, 528, A72
Heyer M., Soler J. D., Burkhart B., 2020, MNRAS, 496, 4546
Hoang T. D. et al., 2022, ApJ, 929, 27
Hollins J. F., Sarson G. R., Evirgen C. C., Shukurov A., Fletcher A., Gent F. A., 2018, preprint (arXiv:1809.01098)
Hopkins P. F., 2012, MNRAS, 423, 2037
Hopkins P. F., 2013, MNRAS, 430, 1653
Hopkins P. F., Squire J., Chan T. K., Quataert E., Ji S., Kereš D., Faucher-Giguère C.-A., 2021, MNRAS, 501, 4184
Hu Y. et al., 2019, Nat. Astron., 3, 776
Hunter J. D., 2007, Comput. Sci. Eng., 9, 90
Hwang J. et al., 2021, ApJ, 913, 85
Iroshnikov P. S., 1964, SvA, 7, 566
Jaupart E., Chabrier G., 2021, ApJ, 922, L36
Jin K., Salim D. M., Federrath C., Tasker E. J., Habe A., Kainulainen J. T., 2017, MNRAS, 469, 383
Jokipii J. R., Parker E. N., 1968, Phys. Rev. Lett., 21, 44
Karlsson T., Bromm V., Bland-Hawthorn J., 2013, Rev. Mod. Phys., 85, 809
Kitsionas S. et al., 2009, A&A, 508, 541
Körtgen B., Soler J. D., 2020, MNRAS, 499, 4785
Körtgen B., Federrath C., Banerjee R., 2017, MNRAS, 472, 2496
Kraichnan R. H., 1965, Phys. Fluids, 8, 1385
Kriel N., Beattie J. R., Seta A., Federrath C., 2022, MNRAS, 513, 2457
Kritsuk A. G., Ustyugov S. D., Norman M. L., 2017, New J. Phys., 19, 065003
Krumholz M. R., Burkhart B., 2016, MNRAS, 458, 1671
Krumholz M. R., Federrath C., 2019, Frontiers Astron. Space Sci., 6, 7
Krumholz M. R., McKee C. F., 2005, ApJ, 630, 250
Krumholz M. R., Ting Y.-S., 2018, MNRAS, 475, 2236
Krumholz M. R., Crocker R. M., Xu S., Lazarian A., Rosevear M. T., Bedwell-Wilson J., 2020, MNRAS, 493, 2817
Landau L. D., Lifshitz E. M., 1959, Course of Theoretical Physics. Vol. 6: Fluid Mechanics. Pergamon Press, Oxford
Lazarian A., Beresnyak A., 2006, MNRAS, 373, 1195
Lazarian A., Yuen K. H., Ho K. W., Chen J., Lazarian V., Lu Z., Yang B., Hu Y., 2018, ApJ, 865, 46
Lazarian A., Yuen K. H., Pogosyan D., 2020, ApJ, preprint (arXiv:2002.07996)
Lazarian A., Yuen K. H., Pogosyan D., 2022, ApJ, preprint (arXiv:2204.09731)
Li H.-B., Fang M., Henning T., Kainulainen J., 2013, MNRAS, 436, 3707
Li H.-B., Goodman A., Sridharan T. K., Houde M., Li Z.-Y., Novak G., Tang K. S., 2014, in Beuther H., Klessen R. S., Dullemond C. P., Henning T., eds, Protostars and Planets VI. Univ. Arizona Press, Tucson, AZ, p. 101
Li P. S., Lopez-Rodriguez E., Ajeddig H., André P., McKee C. F., Rho J., Klein R. I., 2022, MNRAS, 510, 6085
Liu J., Qiu K., Zhang Q., 2022, ApJ, 925, 30

Lu Z.-J., Pelkonen V.-M., Padoan P., Pan L., Haugbølle T., Nordlund Å., 2020, ApJ, 904, 58
Lyra W., Umurhan O. M., 2019, PASP, 131, 072001
McKee C. F., Stacy A., Li P. S., 2020, MNRAS, 496, 5528
Menon S. H., Federrath C., Klaassen P., Kuiper R., Reiter M., 2021, MNRAS, 500, 1721
Mocz P., Burkhart B., 2018, MNRAS, 480, 3916
Nam D. G., Federrath C., Krumholz M. R., 2021, MNRAS, 503, 1138
Oliphant T., 2006, Guide to NumPy. Trelgol Publishing, USA
Omukai K., Tsuribe T., Schneider R., Ferrara A., 2005, ApJ, 626, 627
Orkisz J. H. et al., 2017, A&A, 599, A99
Padoan P., Nordlund Å., 2011, ApJ, 730, 40
Padoan P., Nordlund P., Jones B. J. T., 1997, Commmun. Konkoly Obser. Hungary, 100, 341
Padoan P., Pan L., Haugbølle T., Nordlund Å., 2016, ApJ, 822, 11
Panopoulou G. V., Psaradaki I., Tassis K., 2016, MNRAS, 462, 1517
Parker E. N., 1970, ApJ, 160, 383
Parker E. N., 1979, The International Series of Monographs on Physics: Cosmical Magnetic Fields. Their origin and their Activity. Clarendon Press, Oxford
Peek J. E. G., Burkhart B., 2019, ApJ, 882, L12
Reynolds O., 1895, Philos. Trans. R. Soc. Lond. A, 186, 123
Rincon F., 2019, J. Plasma Phys., 85, 205850401
Sampson M. L., Beattie J. R., Krumholz M. R., Crocker R. M., Federrath C., Seta A., 2022, preprint (arXiv:2205.08174)
Saydjari A. K., Portillo S. K. N., Slepian Z., Kahraman S., Burkhart B., Finkbeiner D. P., 2021, ApJ, 910, 122
Schekochihin A. A., 2020, preprint (arXiv:2010.00699)
Schekochihin A. A., Cowley S. C., Hammett G. W., Maron J. L., McWilliams J. C., 2002, New J. Phys., 4, 84
Schekochihin A. A., Cowley S. C., Taylor S. F., Maron J. L., McWilliams J. C., 2004, ApJ, 612, 276
Schneider N. et al., 2013, ApJ, 766, L17
Schober J., Schleicher D., Federrath C., Klessen R., Banerjee R., 2012, Phys. Rev. E, 85, 026303
Schober J., Schleicher D. R. G., Federrath C., Bovino S., Klessen R. S., 2015, Phys. Rev. E, 92, 023010
Schruba A., Kruijssen J. M. D., Leroy A. K., 2019, ApJ, 883, 2
Seta A., Federrath C., 2020, MNRAS, 499, 2076
Seta A., Federrath C., 2021a, Phys. Rev. Fluids, 6, 103701
Seta A., Federrath C., 2021b, MNRAS, 502, 2220
Seta A., Bushby P. J., Shukurov A., Wood T. S., 2020, Phys. Rev. Fluids, 5, 043702
Sharda P. et al., 2022, MNRAS, 509, 2180
Skalidis R., Tassis K., 2021, A&A, 647, A186
Skalidis R., Sternberg J., Beattie J. R., Pavlidou V., Tassis K., 2021a, A&A, 656, A118 (S+2021)
Skalidis R. et al., 2021b, A&A, preprint (arXiv:2110.11878)
Soler J. D., Hennebelle P., Martin P. G., Miville-Deschênes M. A., Netterfield C. B., Fissel L. M., 2013, ApJ, 774, 128
Sridhar S., Goldreich P., 1994, ApJ, 432, 612
Stroustrup B., 2013, The C++ Programming Language, 4th edn. Addison-Wesley, Upper Saddle River, NJ
Subramanian K., 2016, Rep. Progress Phys., 79, 076901
Subramanian K., 2019, Galaxies, 7, 47
Sur S., Schleicher D. R. G., Banerjee R., Federrath C., Klessen R. S., 2010, ApJ, 721, L134
van der Walt S. et al., 2014, PeerJ, 2, e453
Virtanen P. et al., 2020, Nat. Methods, 17, 261
Waagan K., Federrath C., Klingenberg C., 2011, J. Comput. Phys., 230, 3331
Wibking B. D., Krumholz M. R., 2021, preprint (arXiv:2105.04136)
Wolfire M. G., Hollenbach D., McKee C. F., Tielens A. G. G. M., Bakes E. L. O., 1995, ApJ, 443, 152
Xu S., Lazarian A., 2016, ApJ, 833, 215
Yuen K. H., Lazarian A., 2020, ApJ, 898, 66
Yun H.-S. et al., 2021, ApJ, 921, 31
Zel'dovich Y. B., 1957, Sov. Phys. JETP, 4, 460
Zhou J.-X., Li G.-X., Chen B.-Q., 2022, MNRAS, 513, 638
Zweibel E. G., McKee C. F., 1995, ApJ, 439, 779

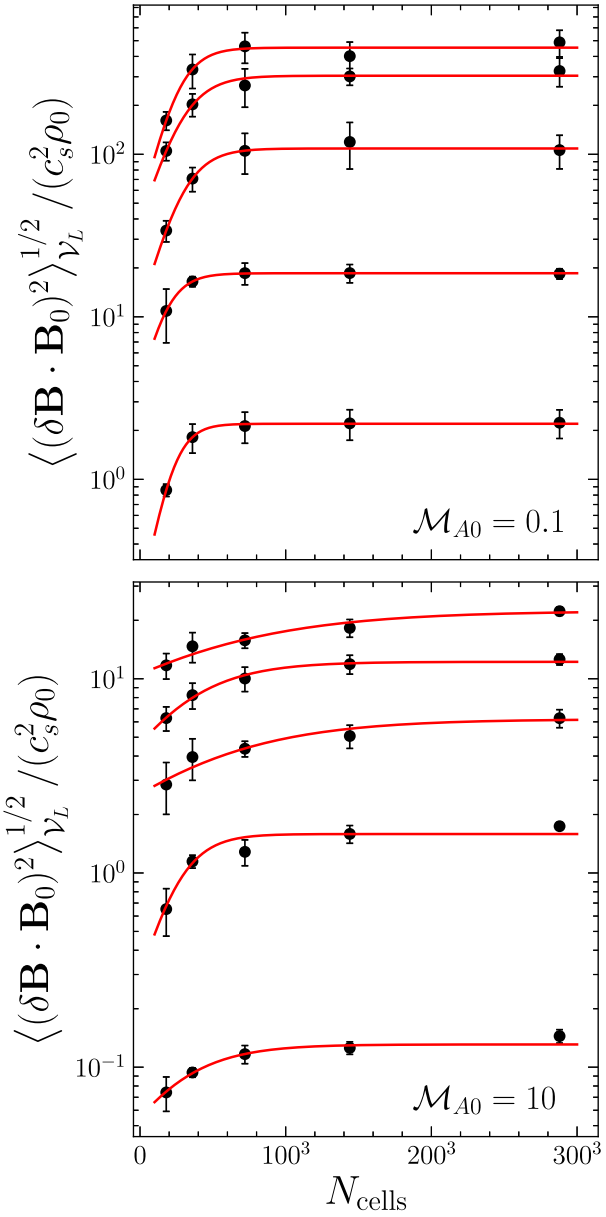

Figure A1. The coupling term, as discussed in Section 3, as a function of numerical grid resolution for the `MA01` and `MA10` simulations, from Table 1. Each curve shows a different set of $\mathcal{M}$, varying from $\mathcal{M} = 0.5$, corresponding to data lowest on the coupling term axis, up to $\mathcal{M} = 10$, at the top.

APPENDIX A: NUMERICAL CONVERGENCE

All of the results presented in this study are numerically converged in grid resolution. We ensure that this is the case by computing all of our statistics on simulations with discretizations 18^3, 36^3, 72^3, 144^3, and 288^3. To highlight the convergence trends, we fit a general logistic function to the data,

$$f(N_{\rm cells}) = \frac{f_\infty^+}{1 + \exp\{\alpha(N_{\rm cells} - N_0)\}} + f_\infty^-, \tag{A1}$$

where α controls the rate in which the function converges to either f_∞^-, for monotonically decreasing functions ($\alpha > 0$), or $f_\infty^+ + f_\infty^-$ for monotonically increasing functions ($\alpha < 0$), and N_0 shifts the function along the $N_{\rm cells}$ axis.

We plot $\left\langle (\delta \boldsymbol{B} \cdot \boldsymbol{B}_0)^2 \right\rangle_{\mathcal{V}}^{1/2}$ as a function of grid cells, $N_{\rm cells}$, for the $\mathcal{M}_{\rm A0} = 0.1$ (top) and $\mathcal{M}_{\rm A0} = 10$ (bottom) simulation ensembles,

listed in Table 1, in Fig. A1, showcasing representative examples for the super- and sub-Alfvénic simulations. Naturally, the simulations are organized into constant $\mathcal{M}$, with low $\mathcal{M}$ corresponding to the smallest $\langle(\delta\boldsymbol{B}\cdot\boldsymbol{B}_0)^2\rangle_{\mathcal{V}}^{1/2}$ and vice versa for high $\mathcal{M}$. For all simulations in Fig. A1, 144^3 grid resolution is sufficient for numerical convergence. This is because, unlike power spectra or other two-point statistics, which require $>4096^3$ resolutions to converge properly (Federrath 2013; Federrath et al. 2021), the variance of the fields convergence quickly. This is because the low-k modes contain most of the power in the stochastic fields, and hence $\gtrsim 144^3$ is sufficient to resolve the largest contributions to the second moments of the fields. In the main text of this study, we use simulations discretized with 288^3 cells, to ensure that the above condition is met.

APPENDIX B: ANISOTROPY OF THE MAGNETIC AND VELOCITY FLUCTUATIONS

In Section 5, we modify the energy balance relations based on the anisotropy of the rms magnetic and velocity fluctuations. If the turbulence is isotropic (with respect to the large-scale field), we have $\sqrt{3}\,\langle\delta B_\parallel^2\rangle_{\mathcal{V}}^{1/2} = \langle\delta B^2\rangle_{\mathcal{V}}^{1/2}$. However, sub-Alfvénic mean-field turbulence is highly anisotropic on all scales, in the velocity, magnetic field, and density statistics (Beattie & Federrath 2020). Here we specifically plot the fluctuations, showing $\langle\delta B_\perp^2\rangle_{\mathcal{V}}^{1/2}$ as a function of $\langle\delta B_\parallel^2\rangle_{\mathcal{V}}^{1/2}$ in Fig. B1 and $v_\parallel$ as a function of $\langle\delta v_\perp^2\rangle_{\mathcal{V}}^{1/2}$ in Fig. B2, all averaged over five correlations times of the turbulent forcing function, discussed in Section 2.

Naturally, the most anisotropic rms statistics come from the strongly sub-Alfvénic simulations, which can be as extreme as $\langle\delta B_\perp^2\rangle_{\mathcal{V}}^{1/2} = (1/3)\,\langle\delta B_\parallel^2\rangle_{\mathcal{V}}^{1/2}$ and $(1/3)\,\langle\delta v_\perp^2\rangle_{\mathcal{V}}^{1/2} \le \langle\delta v_\parallel^2\rangle_{\mathcal{V}}^{1/2} \le (2/3)\,\langle\delta v_\perp^2\rangle_{\mathcal{V}}^{1/2}$. In the mean-field coordinate system that we work in through this study, $\langle\delta B^2\rangle_{\mathcal{V}}^{1/2} = \sqrt{\langle\delta B_{\perp,1}^2\rangle_{\mathcal{V}} + \langle\delta B_{\perp,2}^2\rangle_{\mathcal{V}} + \langle\delta B_\parallel^2\rangle_{\mathcal{V}}}$, and likewise for the velocity. For $(1/3)\,\langle\delta B_\parallel^2\rangle_{\mathcal{V}}^{1/2} \le \langle\delta B_\perp^2\rangle_{\mathcal{V}}^{1/2} \le (2/3)\,\langle\delta B_\parallel^2\rangle_{\mathcal{V}}^{1/2}$, the total magnitude is then related to $\langle\delta B_\parallel^2\rangle_{\mathcal{V}}^{1/2}$ via the inequality,

$$\frac{\sqrt{11}}{3}\,\langle\delta B_\parallel^2\rangle_{\mathcal{V}}^{1/2} \le \langle\delta B^2\rangle_{\mathcal{V}}^{1/2} \le \frac{\sqrt{17}}{3}\,\langle\delta B_\parallel^2\rangle_{\mathcal{V}}^{1/2}, \tag{B1}$$

and likewise for $\langle\delta v^2\rangle_{\mathcal{V}}^{1/2}$ and $\langle\delta v_\perp^2\rangle_{\mathcal{V}}^{1/2}$,

$$\frac{\sqrt{19}}{3}\,\langle\delta v_\perp^2\rangle_{\mathcal{V}}^{1/2} \le \langle\delta v^2\rangle_{\mathcal{V}}^{1/2} \le \frac{\sqrt{22}}{3}\,\langle\delta v_\perp^2\rangle_{\mathcal{V}}^{1/2}. \tag{B2}$$

Because the coefficients are so close to unity ($\sqrt{11}/3 \approx 1.11$, $\sqrt{17}/3 \approx 1.37$) this demonstrates that in the sub-Alfvénic mean-field regime it is the parallel magnetic field fluctuations and perpendicular velocity fluctuations that dominate the respective total fluctuations.

In Fig. B3, we plot the joint magnetic field fluctuation distribution for the super-Alfvénic simulation, `M2MA10`, to contrast the sub-Alfvénic case in Fig. 2. The strong anisotropy in the sub-Alfvénic joint PDF disappears in the super-Alfvénic data, and the fluctuations become spherically symmetric and hence isotropic.

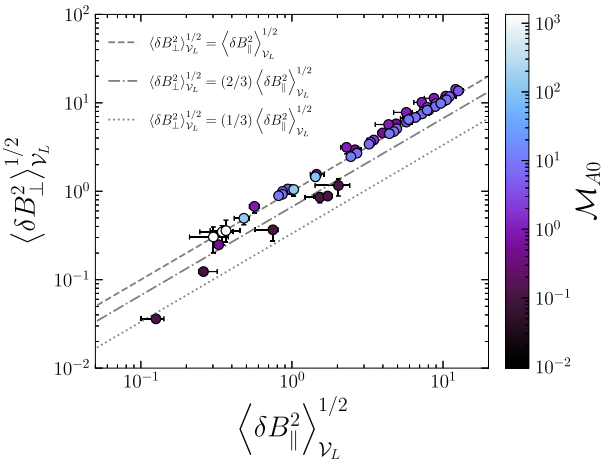

Figure B1. The rms perpendicular magnetic field fluctuations, $\langle\delta B_\perp^2\rangle_{\mathcal{V}}^{1/2}$, as a function of the rms parallel magnetic field fluctuations, $\langle\delta B_\parallel^2\rangle_{\mathcal{V}}^{1/2}$, coloured by $\mathcal{M}_{A0}$. We show contours at $\langle\delta B_\perp^2\rangle_{\mathcal{V}}^{1/2} = \langle\delta B_\parallel^2\rangle_{\mathcal{V}}^{1/2}$, $\langle\delta B_\perp^2\rangle_{\mathcal{V}}^{1/2} = (2/3)\,\langle\delta B_\parallel^2\rangle_{\mathcal{V}}^{1/2}$, and $\langle\delta B_\perp^2\rangle_{\mathcal{V}}^{1/2} = (1/3)\,\langle\delta B_\parallel^2\rangle_{\mathcal{V}}^{1/2}$, illustrating how the rms magnetic field fluctuations become anisotropic in the $\mathcal{M}_{A0} < 1$ regime.

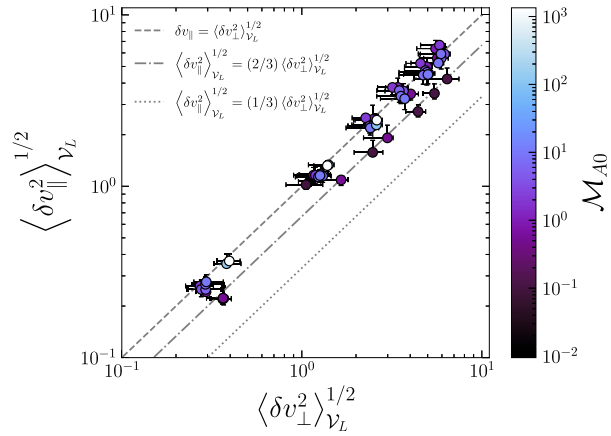

Figure B2. The same as Fig. B1, but for the rms velocity fluctuations perpendicular and parallel to $\boldsymbol{B}_0$. Note, compared to Fig. B1 the anisotropy is inverted between the parallel and perpendicular directions.

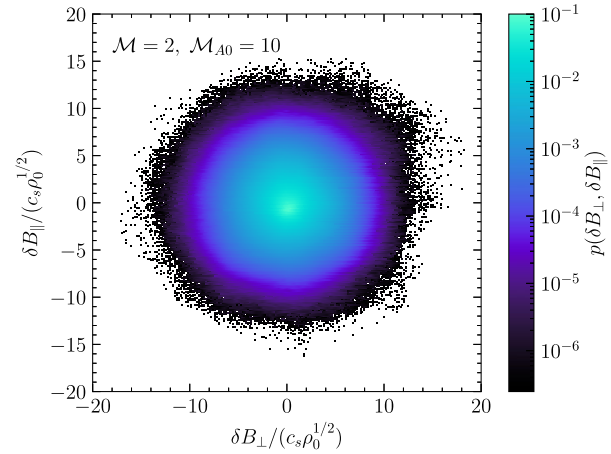

Figure B3. The same as Fig. 2, but for the `M2MA10` simulation, highlighting the global, isotropic nature of the magnetic field fluctuations in the super-Alfvénic regime.

APPENDIX C: AVERAGING AS A FUNCTION OF LENGTH SCALE

In Section 6, we compute $\langle \delta \boldsymbol{B} \cdot \boldsymbol{B}_0 \rangle$ and $\left\langle \delta \boldsymbol{B}^2 \right\rangle^{1/2}$ as a function of length scale in the turbulence for the `M2MA001` and `M2MA10` simulations, as well as $\mathcal{M}_{\rm A0}$ and $\mathcal{M}_{\rm A,turb}$ for the `M2MA10` simulation. To do this we pick a random coordinate (x_1, x_2, x_3), in the three-dimensional simulation, and expand a set of concentric i spheres,

$$\mathcal{S}_i = \{(x, y, z) \in \mathcal{V}_{\mathcal{L}} \mid (x - x_1)^2 + (y - x_2)^2 + (z - x_3)^2 = (\ell_i/2L)^2\}, \tag{C1}$$

over a range of diameters, $\ell_i/L \in [0, 1]$. $\mathcal{S}_i$ is then our filter, and for each ℓ_i/L we compute the convolved field variables,

$$f^*(\ell_i/L) = \int_{\mathcal{V}_{\mathcal{L}}} \mathrm{d}f \, \mathcal{S}_i f(x, y, z), \tag{C2}$$

where $f(x, y, z)$ is either $\delta \boldsymbol{B} \cdot \boldsymbol{B}_0$, $\delta \boldsymbol{B}^2$, all of the components for $\mathcal{M}_{\rm A0}$ and $\mathcal{M}_{\rm A,turb}$ as per our definitions in Section 5, or for $\left\langle (\delta \boldsymbol{B} \cdot \boldsymbol{B}_0)^2 \right\rangle_{\mathcal{V}}^{1/2} / (2 c_{\rm s}^2 \rho_0 \pi \mathcal{M}^2)$, and f^* is corresponding length-dependent field variable. Next, we compute the volume averages, $\langle f^*(\ell_i/L) \rangle_{\mathcal{V}}$, where $\mathcal{V}$ is the volume $(4/3)\pi(\ell_i/2L)^3$, for each ℓ_i/L. Finally, we independently compute the velocity power spectra and correlation scale, $\ell_{\mathrm{cor},\,v}$, of the simulation boxes using equation (32), allowing us to transform all of the length scale units into correlation scales. We show $\left\langle \delta \boldsymbol{B} \cdot \boldsymbol{B}_0 (\ell_i/\ell_{\mathrm{cor},v}) \right\rangle_{\mathcal{V}}$ and $\left\langle \delta \boldsymbol{B}^2 (\ell_i/\ell_{\mathrm{cor},v}) \right\rangle_{\mathcal{V}}$ for a representative sub-Alfvénic and super-Alfvénic simulation in Fig. 10.

This paper has been typeset from a TEX/LATEX file prepared by the author.